USING AXODES TO COMPARE BIOKINEMATIC DATA MEASURED WITH BONE- AND SKIN-MOUNTED MARKERS

by

JENS OLOF MATTIAS KARLSSON

B.S. in Physics, Massachusetts Institute of Technology (1988)

SUBMITTED TO THE DEPARTMENT OF
MECHANICAL ENGINEERING
IN PARTIAL FULFILLMENT OF THE REQUIREMENTS
FOR THE DEGREE OF

MASTER OF SCIENCE IN MECHANICAL ENGINEERING

at the

MASSACHUSETTS INSTITUTE OF TECHNOLOGY

May, 1990

Signature of Author_____
Department of Mechanical Engineering
May 11, 1990

Certified by_____
Professor Robert W. Mann
Thesis Supervisor

Accepted by_____
Professor Ain A. Sonin
Chairman, Departmental Committee on Graduate Studies

USING AXODES TO COMPARE BIOKINEMATIC DATA MEASURED WITH BONE- AND SKIN-MOUNTED MARKERS

by

JENS OLOF MATTIAS KARLSSON

Submitted to the Department of Mechanical Engineering
on May 11, 1990 in partial fulfillment of the requirements
for the Degree of Master of Science in Mechanical Engineering.

ABSTRACT

Two schemes for attaching skin-mounted markers used in a photogrammetric motion measurement system, were evaluated by comparing the measured kinematics with directly measured skeletal motion data. The direct measurements were obtained by mounting plexiglass arrays of markers on skeletal pins at the femur and tibia of the subject. The external mounting methods were: (1) rigid, acrylic frames strapped over bony prominences, and (2) molded, plastic forms held on the subject with a vascular stocking. Experiments had previously been performed by Murphy (1984), acquiring *in vivo* kinematic data with each attachment method, for normal gait and voluntary swing of the knee, using the same subject.

In order to maintain consistency in the data representation between experiments, the instantaneous helical axis (IHA) was calculated, and axodes were generated. The axode shape does not require alignment of reference coordinate axes for the different experiments.

The IHA calculation requires differentiation of the kinematic data, and thus necessitates noise reduction. Data were processed with the TRACK software; a set of optimal processing parameters were selected. Three-dimensional marker position data were smoothed using a dynamic programming smoother with generalized cross-validation. A 3-point finite differences filter was used to calculate the necessary rigid body velocities.

Error analysis indicated that errors in the IHA calculation were on the order of 0.1 in the components of the direction unit vector, and on the order of 2 cm in the components of the IHA location vector.

For swing experiments, axodes from the external mounting methods were similar to the axode obtained from the directly measured data, but some deviations were present, indicating artifactual soft tissue motion.

Skin-mounted markers could not accurately measure all features of stance-phase kinematics in gait. Type 2 mounting yielded better results than Type 1 mounting.

Thesis Supervisor: Professor Robert W. Mann
Title: Whitaker Professor of Biomedical Engineering
Department of Mechanical Engineering

Acknowledgements

I would like to thank everybody who has helped with or otherwise contributed to this work. I am especially grateful to the following people:

Professor Mann, who gave me the opportunity to work in the Newman Lab, and was always available for friendly and helpful advice.

Mike Murphy, for doing the experiments, and for introducing me to screws and biomechanics. Thanks for your guidance and support, and for finding time to help even when your own work was overwhelming.

Pat Lord, for developing the IRIS graphics software, with which the three-dimensional ruled surfaces where displayed and printed.

Pete Mansfield, for his help in explaining various aspects of the TRACK hardware.

Clark Dohrmann, for his guidance in installing and debugging the smoothing algorithm.

Bengt and Monica, for being great parents, and for always supporting me in everything I do – tack för allt !

Sheri, for everything you've done for me. Thank you for being patient with me through this time, and for always being my friend. I can't begin to let you know how much I appreciate your presence in my life. Jag älskar dig...

This work was supported in part by the U.S. Dept. of Education, National Institute on Disability and Rehabilitative Research Grant No. H133E80024.

This thesis was performed in the Eric P. and Evelyn E. Newman Laboratory for Biomechanics and Human Rehabilitation in the Department of Mechanical Engineering at the Massachusetts Institute of Technology.

Contents

List of Figures

List of Tables

Chapter 1

Introduction

The knee joint is the largest, most complex of the synovial joints in the human body; it is also the joint most often injured and most often surgically encountered. Yet, an accurate, predictive, mathematical model of the knee is not available. The development of such a model requires a description of the kinematics of the knee.

In any study of joint kinematics, it is crucial to have precise data on the relative motion of the body segments linked by the joint. The analysis and modelling of biological joints, the evaluation of the effectiveness of reconstructive orthopaedic surgery, the diagnosis of pathology, and the design of prostheses are some important applications which require a consistent, quantitative description of relative skeletal kinematics. Due to problems in both methodology and choice of kinematic representation, most biokinematic data reported in the literature to date are inconsistent and suitable only for gross qualitative analyses. This work seeks to develop a rigorous, quantitative approach to kinematic studies of biological joints.

Two fundamental problems inherent to biokinematics are how to measure *in vivo* skeletal motion and how to assign the coordinate frames to which the data will be referenced.

1.1 Measurement of Skeletal Kinematics

Problems in data acquisition can be divided into two main areas of concern: First, the restriction to use skin-mounted markers; although some *in vivo* experiments using markers mounted on skeletal pins have been reported [17, 9], these techniques are not practical for clinical or extensive research use. Since the goal is to measure skeletal kinematics, it is important to know to what extent the skeletal information is available when using markers not directly affixed to the bone.

The second problem in methodology is the widespread use of measurement systems which make *a priori* assumptions about the joint kinematics. Experiments in which markers are placed over "joint centers" not only assume that the motion is planar and in the plane of the markers, but also that the joint has one single degree of freedom and that translational motion can be neglected. In view of the lack of a comprehensive, precise model of the knee joint, none of these assumptions can be justified. In addition, some of the assumptions, such as the supposed planarity of knee kinematics, have been repeatedly contradicted [10, 9, 17, 20].

A rigorous method for acquiring joint kinematic data must proceed by defining at each limb a body-fixed coordinate system (BFCS), then observing the full 6 degree of freedom rigid body motion of the body-fixed frames relative to each other. Experimentally, this can be achieved by attaching to the body segments of interest (femur and tibia for knee kinematics) an array of three or more markers, from which the location and orientation of each BFCS can be calculated with respect to the laboratory reference frame. Relative kinematics are obtained by designating one BFCS as a reference coordinate system, the other as a "moving" BFCS, then performing a transformation of the moving frame kinematic data from the laboratory frame basis to the reference frame BFCS basis.

1.2 Representations of Kinematic Data

Typical representations of biokinematic data are zeroeth order: they use only position and orientation data and do not depend on time-derivatives. As such, these representations are extremely sensitive to the definitions of both reference and moving BFCS relative to the corresponding skeletal segments. Usually, "anatomical" coordinate systems are referenced to skeletal landmarks. This process is error-prone and is a source of imprecision and inconsistency in results and interpretations. Since consistency is imperative when comparing data, the issue warrants serious attention. The problem can be circumvented by employing kinematic representations which use first and higher order derivatives of position and orientation data.

Zeroeth order representations include Euler angles, used commonly in different variations, also alternative systems such as the representation developed by Grood and Suntay [6], and finite helical axis methods [7]. These descriptions have in common that results are dependent on how both the reference BFCS and the moving BFCS are defined. No standards exist for defining these body-fixed frames, and even if a standard were available, empirical coordinate system definitions would not be reliable. As a result, reported findings are inconsistent, interpretations are questionnable, and comparative analyses cannot be meaningful.

Instantaneous helical axis (IHA) methods have been shown to constitute a powerful first order kinematic representation [8]. The IHA coincides with the instantaneous axis of rotation and is independent of how the moving BFCS is defined. Associated with each IHA is an instantaneous angular speed about it and an instantaneous linear speed along it; these quantities are invariants of the motion and do not depend on either coordinate system definition. A general finite motion is represented by an IHA locus, the axode, which again is independent of the moving BFCS. The location and orientation of the axode will depend on how the reference coordinate system is defined, but the shape of the axode is independent of both reference and moving BFCS definition.

The axode shape can be characterized quantitatively using dual differential geometry.

Shape parameters such as dual curvature, torsion and arclength are invariants of the motion, which together with the instantaneous linear and angular speeds, completely characterize the joint kinematics. This higher order representation is totally independent of BFCS definition.

By using first and higher order methods, problems due to inconsistent BFCS definitions can be avoided. However, these representations require differentiation of experimental data – the resulting amplification of high frequency systematic noise may be prohibitive.

1.3 Objectives

This work addresses problems in acquiring and representing kinematic data for the human knee joint. Data presented are from a set of three experiments previously performed at the Massachusetts Institute of Technology. Using the same subject and same protocol, 6 degree of freedom biomotion data were obtained using bone-mounted markers in a reference experiment [17], and using two different methods for externally mounting markers [15]. By analyzing this data, a number of important questions can be answered.

The research presented here concerns itself with whether or not instantaneous helical axis methods can be applied to biokinematic data with sufficient accuracy; and whether or not externally mounted markers are adequate indicators of skeletal motion.

Chapter 2

Experiments

Experiments were conducted by Murphy in 1985 [15] with the purpose of detecting differences between bone- and skin-mounted marker systems. The experiments were performed using two different schemes for mounting arrays of markers on the skin. In an earlier study (1984) by Murphy [17], kinematic data had been acquired using marker arrays mounted directly to the skeletal segments via bone-pins. Assuming the kinematics of the biological mechanism are relatively constant for a given task, differences between data for the various mounting methods can be attributed to artifactual soft tissue motion.

This work focusses on the latter study, in which externally mounted marker arrays were used. Some data from the bone pin experiments are included for comparisons; for a detailed description of the bone pin experiments and results, see Murphy, 1990 [13].

2.1 The TRACK system

The experimental data were collected using the Telemetered Real-time Acquisition of Kinematic (TRACK) data system [2, 18]. TRACK consists of a Selspot (Selective Electronics, Partille, Sweden) kinematic acquisition system coordinated with a Kistler (Kistler Instrumente AG, Winterthur, Switzerland) force platform, and an extensive software package. The markers used by TRACK are small infrared LED clusters.

The Selspot II opto-electronic cameras measure coordinates (u, v) of the center of intensity of infrared light on the camera image plane. Digitization of u and v divides the

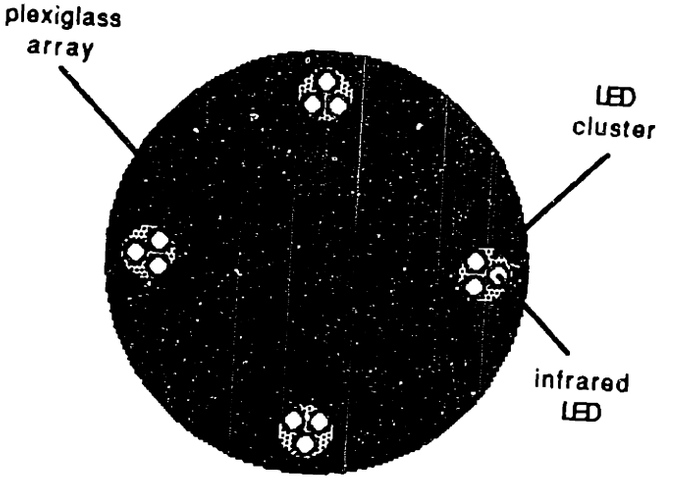

Figure 2.1: TRACK array

detector in the image plane into a grid: each side has 4096 divisions, the length of one of which defines one Selspot Unit (S.U.).

If the light is from a single point-like source, then the (u, v)-coordinates correspond to the location of the source image. By using two cameras, the three-dimensional location of the source in the laboratory coordinate frame can be reconstructed with stereophotogrammetric techniques.

To study joint kinematics in a general way, the femur and tibia are modelled as rigid bodies, and measurement of the full six degree of freedom motion of each body segment is necessary. Since the position and orientation of a rigid body are completely determined by the location of three noncolinear points on the body, plexiglass arrays containing four LED clusters (see Fig. 2.1) were attached to each limb for acquisition of kinematic data. The bone-mounted arrays used in the 1984 study contained six markers each.

Because the Selspot system can only detect the position of one point source at a time, a multiplexing scheme is used to pulse and record each source sequentially. By using pulses of short duration and pulsing rapidly, it is possible to stream through a

large number of point sources in short periods of time. Each such stream through all point sources is known as one *Selspot frame.* In the experiments using external mounting, data were collected at a sampling rate of 285.7 Hz.

The TRACK software processes the Selspot data, calculating the position x and orientation q of each array for every frame (see Section 4.1).

In measurements of gait, dynamic data from the force platform were sampled at each Selspot frame, in addition to the kinematic data.

2.2 Experiments

In order to determine the effect of soft tissue motion by comparison of kinematic data, the kinematics must be generated by the same underlying mechanism. Thus, the same subject, a young, healthy male with no history of knee pathology, was used for all experiments. To acquire biokinematic data, TRACK arrays were mounted on the foot, shank, thigh and pelvis, with each method of attachment.

Three schemes for array mounting were used: in one, arrays were attached directly to the skeletal segments; in the other two, indirect methods were used, mounting the arrays on the skin. In the case of direct measurements, arrays were mounted on skeletal pins at the greater trochanter, lateral femoral condyle, and mid-shank. The two indirect mounting methods were

Type 1 Rigid, acrylic frames strapped over bony prominences on each skeletal segment.

Type 2 Molded, plastic forms held in place at the pelvis, thigh and foot by a vascular stocking; shank array was attached to a cuff with projections that fit over the malleoli.

Kinematic data were obtained for the subject performing three tasks: (1) Standing erect, with no motion, (2) Voluntary swing of the knee joint through the full range of motion, and (3) Walking at normal speed. Data from the first task are hereafter referred

to as *static* data, the second as *swing* data, and the third as *gait* data. Table 2.1 lists the experiments.

Mounting	Task	Trial	File
Pin	Static	1	14MA30
	Swing	1	14MA32
		2	14MA51
	Gait	1	14MA34
		2	14MA36
		3	14MA37
		4	14MA38
Type 1	Static	1	11JE01
		2	11JE06
		3	11JE12
	Swing	1	11JE02
		2	11JE03
		3	11JE04
		4	11JE05
	Gait	1	11JE07
		2	11JE08
		3	11JE09
		4	11JE10
Type 2	Static	1	11JE20
		2	11JE25
		3	11JE31
	Swing	1	11JE21
		2	11JE22
		3	11JE23
		4	11JE24
	Gait	1	11JE26
		2	11JE27
		3	11JE28
		4	11JE29
		5	11JE30

Table 2.1: List of experiments

Chapter 3

Kinematic Representations

3.1 Rigid Body Motion

Rigid body displacements are combinations of translations and rotations. Translations may be described using vectors; rotations can be represented by *quaternions*.

A quaternion is a complex number

$$q = a\mathbf{i} + b\mathbf{j} + c\mathbf{k} + d, \tag{3.1}$$

with four units i, j, k, 1 and corresponding components a, b, c, d. The rules for multiplication of the units are

$$\begin{gathered} \mathbf{i}^2 = \mathbf{j}^2 = \mathbf{k}^2 = -1 \qquad 1^2 = 1 \\ \begin{array}{lll} \mathbf{ij} = \mathbf{k} & \mathbf{jk} = \mathbf{i} & \mathbf{ki} = \mathbf{j} \\ \mathbf{ji} = -\mathbf{k} & \mathbf{kj} = -\mathbf{i} & \mathbf{ik} = -\mathbf{j}. \end{array} \end{gathered} \tag{3.2}$$

The conjugate of q, denoted $q^\dagger$, is defined

$$q^\dagger = -a\mathbf{i} - b\mathbf{j} - c\mathbf{k} + d. \tag{3.3}$$

A quaternion with a null real component ($d = 0$) is called a *vector quaternion*, and obeys the rules of vector algebra; thus a quaternion may be written formally as the sum of a vector and a real number.

If a quaternion has unit norm, *i.e.*

$$q^\dagger q = q q^\dagger = 1, \tag{3.4}$$

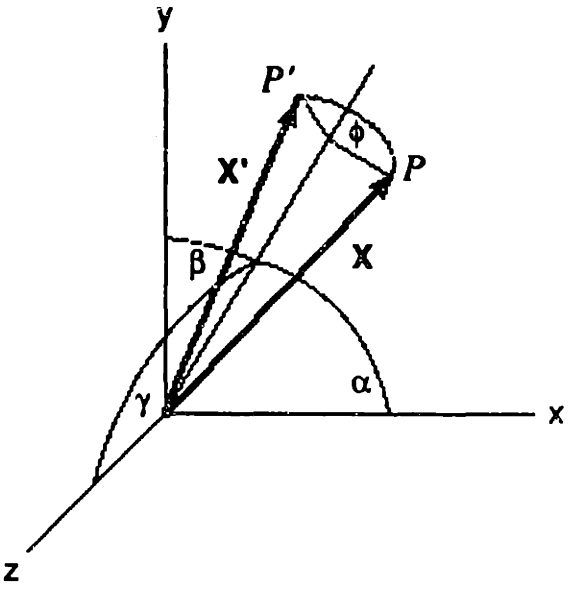

Figure 3.1: Rotation of point P

and if $\mathbf{X}$ is the position vector to a point P, then the operation

$$\mathbf{X}' = q\,\mathbf{X}\,q^{\dagger} \tag{3.5}$$

describes a rotation of P to a new position $\mathbf{X}'$. The quaternion components may be interpreted geometrically by expressing q in the form

$$q = \cos\frac{\phi}{2} + \sin\frac{\phi}{2}(\cos\alpha\,\mathbf{i} + \cos\beta\,\mathbf{j} + \cos\gamma\,\mathbf{k}); \tag{3.6}$$

Equation 3.5 represents a rotation through an angle ϕ about an axis passing through the origin, making angles α, β, and γ with the coordinate axes (see Fig. 3.1).

Thus, if $\mathbf{X}$ is the position vector to a point P on a rigid body, and $\mathbf{X}'$ is the position of P after a general displacement of the body, one has

$$\mathbf{X}' = q\,\mathbf{X}\,q^{\dagger} + \mathbf{x}, \tag{3.7}$$

where $\mathbf{x}$ represents the translation, and q the rotation.

To describe a rigid body motion, $\mathbf{x}$ and q must be specified as functions of time, and a neutral position of the rigid body must be defined. The instantaneous rigid body position is then obtained by using Equation 3.7 to calculate the displacement from the neutral

position at any time. The neutral position is arbitrary, but the choice will affect the values of $\mathbf{x}$ and q. Equivalently, one may define a body fixed coordinate system (BFCS), and take the neutral position to be the rigid body location for which the BFCS coincides with the global reference coordinate system. Then, $\mathbf{x}$ will be the position vector to the origin of the BFCS, and q will represent a rotation about the BFCS origin; the values of both will depend on the BFCS definition.

3.2 Relative Kinematics

In a system of rigid bodies, relative motion is the motion of one rigid body as observed in the BFCS of another. Since the displacement vectors and rotation quaternions which describe the motion of the rigid bodies are measured in a reference coordinate system, relative kinematics are obtained by transforming data from reference frame coordinates to the BFCS coordinates of a rigid body serving as a new reference.

The inverse of operation 3.5 represents a coordinate transformation to a rotated frame: if $\mathbf{X_0}$ is a vector measured in reference frame coordinates, $\mathbf{X_1}$ is the same vector measured in a BFCS with an orientation q_{01} relative to the reference frame, then

$$\mathbf{X_1} = q_{01}^{\dagger}\, \mathbf{X_0}\, q_{01}. \tag{3.8}$$

Similarly, if q_{02} describes the orientation of another BFCS, measured in reference frame coordinates, and $\mathbf{X_2}$ represents $\mathbf{X_0}$ in BFCS coordinates,

$$\mathbf{X_2} = q_{02}^{\dagger}\, \mathbf{X_0}\, q_{02}. \tag{3.9}$$

A transformation from BFCS 1 coordinates to BFCS 2 coordinates would have the form

$$\mathbf{X_2} = q_{12}^{\dagger}\, \mathbf{X_1}\, q_{12}, \tag{3.10}$$

where q_{12} describes the orientation of BFCS 2 measured in BFCS 1 coordinates. Solving for $\mathbf{X_0}$ in 3.8 and substituting into 3.9,

$$\mathbf{X_2} = q_{02}^{\dagger}\, q_{01}\, \mathbf{X_1}\, q_{01}^{\dagger}\, q_{02}; \tag{3.11}$$

so, by inspection,

$$q_{12} = q_{01}^{\dagger}\, q_{02}. \tag{3.12}$$

Thus, given the position vector $\mathbf{x_{01}}$ and orientation q_{01} of BFCS 1, both measured in the reference coordinate system, and likewise $\mathbf{x_{02}}$ and q_{02} for BFCS 2, the relative kinematics are described by

$$\mathbf{x} = q_{01}^{\dagger}(\mathbf{x_{02}} - \mathbf{x_{01}})q_{01} \tag{3.13}$$

$$q = q_{01}^{\dagger}\, q_{02}. \tag{3.14}$$

BFCS 1 is the *reference BFCS*; BFCS 2 will be referred to as the *moving BFCS*. The values of $\mathbf{x}$ and q depend on how both of these body fixed coordinate systems are defined.

3.3 Screws and Helical Axes

As first demonstrated by Chasles (1834), for any finite rigid body displacement there exists a body fixed axis which remains fixed also in the reference frame. This is the *helical* or *screw axis*; the rigid body displacement can be decomposed into a rotation about the axis and a translation along it.

Clifford (1873) developed a notation for representing screw displacements, employing a unit ε with the property

$$\varepsilon^2 = 0. \tag{3.15}$$

A complex number of the form

$$\hat{x} = x + \varepsilon x_0, \tag{3.16}$$

with x and x_0 real, is called a *dual number*. A *screw* is formally expressed as a *dual vector*

$$\hat{\mathbf{A}} = \mathbf{a} + \varepsilon \mathbf{a_0}, \tag{3.17}$$

where $\mathbf{a}$ and $\mathbf{a_0}$ are real vectors. The *theory of transference* establishes correspondence between vectors and screws in such a way that, if the vectors are given a dual form, all the relationships of the vector domain are formally preserved for the screws.

A screw $\hat{\mathbf{A}}$ can be written as the product of a *unit screw* $\hat{\mathbf{R}}$ and a dual magnitude $|\hat{\mathbf{A}}|$:

$$\hat{\mathbf{A}} = |\hat{\mathbf{A}}|\hat{\mathbf{R}}, \tag{3.18}$$

where

$$|\hat{\mathbf{A}}| = (\hat{\mathbf{A}}\cdot\hat{\mathbf{A}})^{1/2}. \tag{3.19}$$

The unit screw

$$\hat{\mathbf{R}} = \mathbf{r} + \varepsilon\mathbf{r_0} \tag{3.20}$$

defines the helical axis: $\mathbf{r}$ is a unit vector parallel to the axis, and $\mathbf{r_0}$ is the *moment* of the axis; if $\mathbf{p}$ is the position vector to a point on the helical axis, then

$$\mathbf{r_0} = \mathbf{p} \times \mathbf{r}. \tag{3.21}$$

For the screw $\hat{\mathbf{A}}$ defined in 3.17,

$$\mathbf{r} = \frac{\mathbf{a}}{|\mathbf{a}|} \tag{3.22}$$

$$\mathbf{p} = \frac{\mathbf{a} \times \mathbf{a_0}}{|\mathbf{a}|^2}, \tag{3.23}$$

and

$$|\hat{\mathbf{A}}| = |\mathbf{a}| + \varepsilon\mathbf{a_0}\cdot\frac{\mathbf{a}}{|\mathbf{a}|}. \tag{3.24}$$

The *instantaneous helical axis* (IHA) is the unit screw corresponding to the *velocity screw*, and represents the helical axis of an infinitesimal displacement. The velocity screw $\hat{\mathbf{V}}$ is defined

$$\hat{\mathbf{V}} = \boldsymbol{\Omega} + \varepsilon\mathbf{V_0}, \tag{3.25}$$

where an Eulerian description of velocities is employed: $\mathbf{V_0}$ is the local rigid body velocity at the origin of the reference frame; $\boldsymbol{\Omega}$ is the angular velocity of the body. Knowing $\hat{\mathbf{V}}$, the IHA can be determined from Equations 3.22 and 3.23. However, typically it is more convenient to represent rigid body velocity data by the motion of a point fixed in the body. For example, given the position $\mathbf{x}$ and the velocity $\mathbf{v}$ of the BFCS origin, and knowing the angular velocity $\boldsymbol{\Omega}$, the IHA

$$\hat{\mathbf{R}} = \mathbf{r} + \varepsilon\mathbf{r_0} \tag{3.26}$$

is specified by

$$\mathbf{r} = \frac{\boldsymbol{\Omega}}{|\boldsymbol{\Omega}|} \tag{3.27}$$

$$\mathbf{p} = \frac{\boldsymbol{\Omega} \times \mathbf{v}}{|\boldsymbol{\Omega}|^2} + \mathbf{x}, \tag{3.28}$$

where, again

$$\mathbf{r_0} = \mathbf{p} \times \mathbf{r}. \tag{3.29}$$

The velocity screw magnitude $|\hat{\mathbf{V}}|$ can be written in the form

$$|\hat{\mathbf{V}}| = \Omega(1 + \varepsilon\mu), \tag{3.30}$$

where the amplitude Ω is the angular speed of rotation about the IHA, and μ is the *pitch* of the screw, *i.e.* the ratio of translational to rotational displacement.

Equations 3.27 and 3.28 can be used to determine the IHA if $\mathbf{x}$, $\mathbf{v}$ and $\boldsymbol{\Omega}$ are known. Given $\mathbf{x}$ and q as functions of time, one has

$$\mathbf{v} = \dot{\mathbf{x}} \tag{3.31}$$

and

$$\boldsymbol{\Omega} = 2\dot{q}q^{\dagger}. \tag{3.32}$$

For relative kinematics, motion is specified by $\mathbf{x_{01}}$, q_{01} and $\mathbf{x_{02}}$, q_{02}. Substituting Equations 3.13 and 3.14 into 3.31 and 3.32 above,

$$\mathbf{v} = q_{01}^{\dagger}(\dot{\mathbf{x}}_{\mathbf{02}} - \dot{\mathbf{x}}_{\mathbf{01}})q_{01} + \dot{q}_{01}^{\dagger}(\mathbf{x_{02}} - \mathbf{x_{01}})q_{01} + q_{01}^{\dagger}(\mathbf{x_{02}} - \mathbf{x_{01}})\dot{q}_{01} \tag{3.33}$$

and

$$\boldsymbol{\Omega} = 2(\dot{q}_{01}^{\dagger}\, q_{02} + q_{01}^{\dagger}\, \dot{q}_{02})q_{02}^{\dagger}\, q_{01}. \tag{3.34}$$

Using 3.13, 3.33 and 3.34 in Equations 3.27 and 3.28, one obtains the IHA of the moving BFCS as measured in the reference BFCS. The values of the IHA components will depend on how the reference BFCS is defined, but will be independent of the moving BFCS definition. The values of the screw amplitude Ω and pitch μ will not depend on either BFCS definition.

3.4 The Axode

The IHA characterizes the motion at an instant in time; a motion of finite duration has associated with it a locus of instantaneous helical axes. This IHA locus is called the *axode*; it is a ruled surface in space.

If the reference and moving rigid bodies are links in a mechanism, the axode corresponding to the relative motion of the links will be fixed in the reference link. The axode will characterize the mechanism, and will be independent of the actual time-history of the motion. The location and orientation of the axode in the reference BFCS depends only on how the reference BFCS is defined with respect to the reference link. However, the shape of the axode does not depend on the definition of the reference BFCS. Also, since each IHA is independent of how the moving BFCS was defined, the axode will be independent of the moving BFCS definition.

Thus, the axode shape is an invariant of the motion: it does not depend on the definition of either the reference or moving BFCS, and it is also not affected by the time-history of the motion.

The shape of the axode is a property of the mechanism. For example, the axode of a mechanism which generates a pure rotational motion is a single, fixed line (see Fig. 3.2). A rolling motion is represented by a planar axode (see Fig. 3.3) [8].

The shape of a ruled surface may be parametrized using differential geometry. Dimentberg developed a system of dual Frenet formulas, from which the dual curvature and torsion can be obtained [3]. These values, when expressed as functions of dual arclength, provide a quantitative, and time-independent description of the shape of an axode.

3.5 Invariants and Comparison

When comparing kinematic data, one must maintain consistency in representing the data. Since it is difficult to consistently define body-fixed axes relative to body segments, biokinematic data should be compared using representations which are independent of

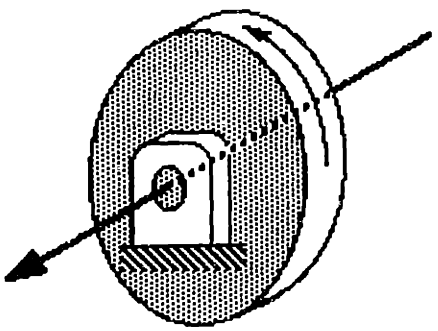

Figure 3.2: Axode for pure rotation

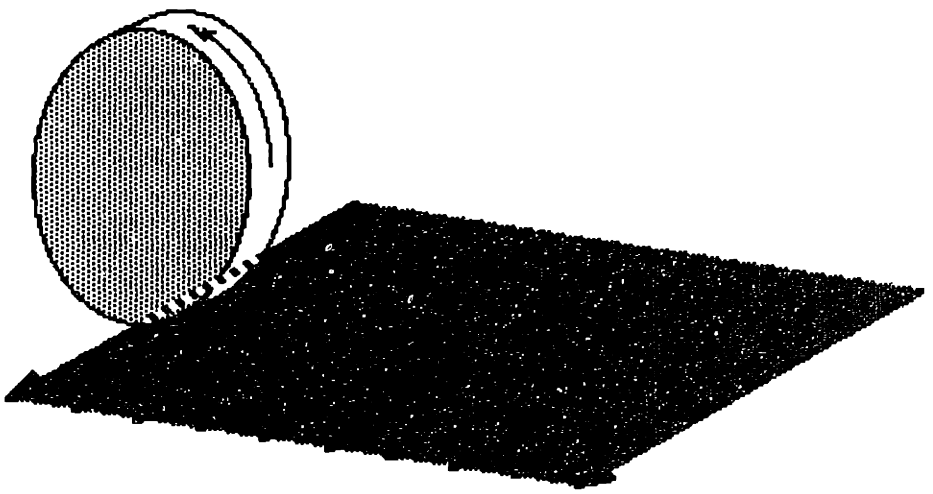

Figure 3.3: Axode for no-slip rolling

BFCS definitions. Quantities which are independent of coordinate frame definitions are called *invariants* of the motion.

For example, the amplitude Ω and pitch μ of the velocity screw are invariants. However, they are not necessarily properties of the mechanism. Consider a mechanism with a single, rotational degree of freedom (Fig. 3.2): although the mechanism is constant, the angular speed Ω may take on different values. Since in our application, the time-history (and equivalently, the speed) of the motion is irrelevant, while a representation of the mechanism itself is desired, invariants like Ω and μ are not appropriate.

By contrast, the axode shape is an invariant which is independent of time, and thus a property of the mechanism. If two mechanisms are identical, so are the corresponding axode shapes; if two mechanisms have axodes of identical shape, they are kinematically equivalent mechanisms. Thus, the axode shape is a representation which is ideally suited for comparison of mechanisms.

The dual curvature and torsion are invariants which parametrize the shape of an axode. However, as demonstrated in previous work, calculation of the dual curvature requires estimates of up to the third time-derivative of rigid body displacement data, and fourth order derivatives are needed for the dual torsion [8]. Since differentiation of experimental data tends to amplify noise levels, errors in the calculated dual curvature and torsion may be prohibitively large.

Although excessive error magnitudes may prevent quantitative characterization of the shape of an axode, other approaches to comparing axode shapes exist. In this research, axodes were compared visually; by graphical rotation of the ruled surfaces, axodes to be compared could be approximately aligned, allowing a visual inspection of similarities and differences in axode shapes.

Chapter 4

Data Processing

Recalling that the purpose of this research is to compare sets of kinematic data using instantaneous helical axes, the goals in processing the experimental data are not only to calculate the necessary rigid body displacements and velocities, but also to reduce noise. Since differentiation is required to determine the velocities, maximizing the smoothness of the data becomes a primary objective. At the same time, one must ensure that the data are not corrupted by the processing. A further constraint is that for any two experiments to be compared, the data must be processed identically, to maintain consistency. The requirements of smoothness, accuracy and consistency are simultaneously satisfied by some optimal processing, which was determined by the procedure described below.

4.1 The TRACK Software

Associated with the TRACK system is an extensive software package, which in part serves to process the data collected from the Selspot II cameras. The algorithms used in this study are based on the original TRACK software developed by Antonsson [1] and revised by Mansfield [11]. A brief outline of the TRACK processing routines is presented here, and is illustrated in block diagram form in Figure 4.1.

Once data have been collected, one may process the data set in its entirety, or select a portion of it for further calculations. For this purpose, a *window* is defined by specifying the first and last frame to be included. It may be used to screen out unreliable data at

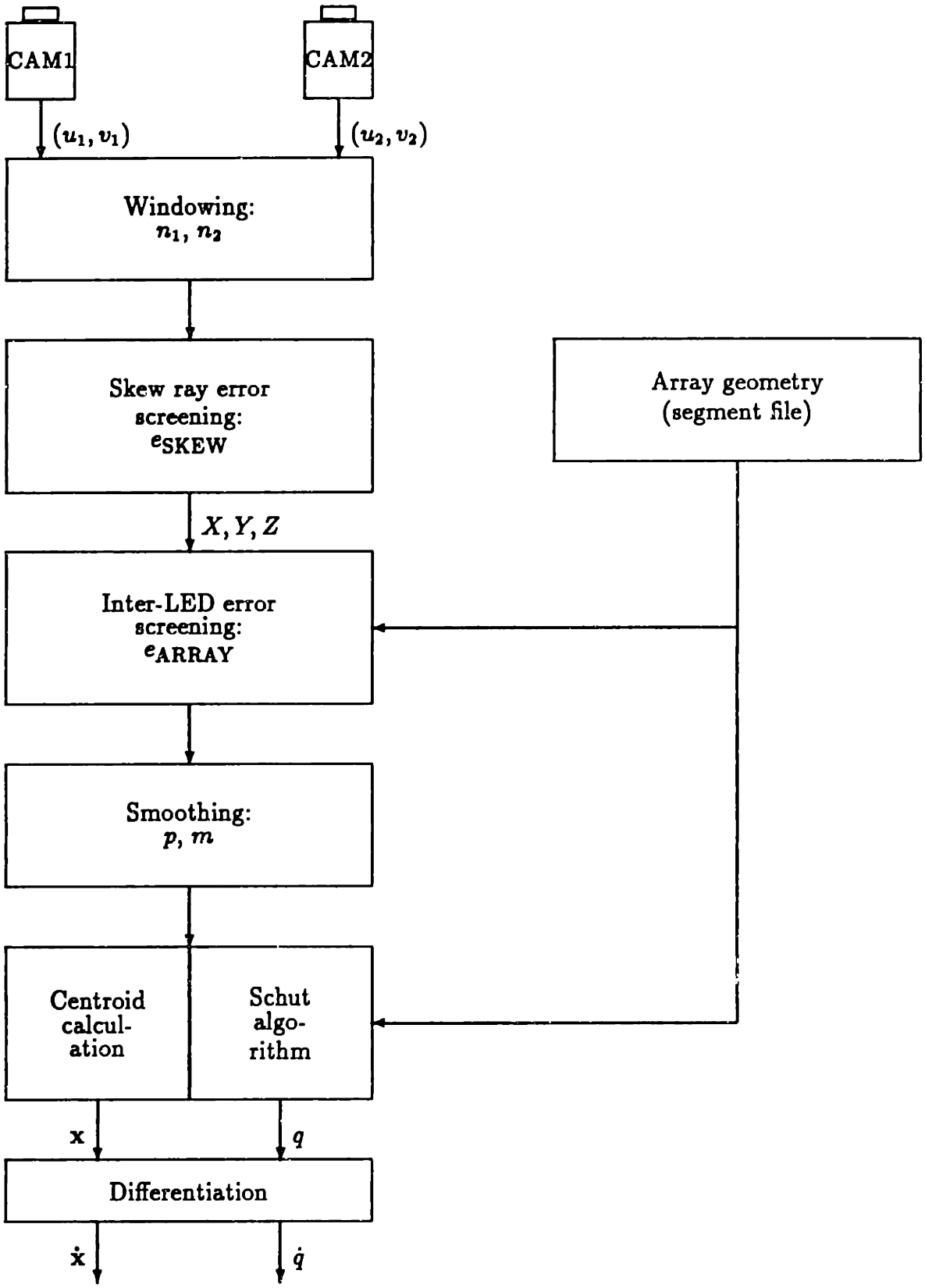

Figure 4.1: TRACK data processing

the beginning or end of an experiment.

The experimental data are initially in the form of coordinate pairs (u, v) representing the LED images detected by the two cameras. From this information, one can reconstruct rays from each camera to the light source. Ideally, these should intersect at the location of the LED. In practice, however, the rays are always skew, and the LED position is taken to be on the common perpendicular, half-way between the two rays. The separation of the rays is a measure of the error in the reconstruction, and is called the *skew ray error*. If the skew ray error is greater than the cutoff level e_{SKEW}, the corresponding measurement is eliminated from the data set. If the skew ray error is less than e_{SKEW}, the 3-dimensional position of the LED is calculated and stored.

Prior to acquiring kinematic data, the geometry of each TRACK array must be specified: the position of every LED on the array, measured in BFCS coordinates, is recorded in a *segment file*. This information is used to determine rigid body kinematics from LED position data.

Before the rigid body location and orientation is calculated, the inter-LED dimensions of all LEDs which lie on the same array are compared to the corresponding dimensions defined in the segment file. The *inter-LED error* is the largest percentage error in the distance between any two LEDs on a given array, and it indicates the amount of distortion in the measured image of the array. If the inter-LED error surpasses the cutoff level e_{ARRAY}, the LED which caused the distortion is eliminated, and a new inter-LED error calculated for the remaining LEDs. Data with error levels below e_{ARRAY} are stored for smoothing and calculation of rigid body kinematics.

The smoothing algorithm used assumes that the noise in the data is additive; this is a reasonable model for the 3-D (3-dimensional) position data. However, since the rigid body orientation calculations are nonlinear in nature, it is not appropriate to smooth rigid body data. For this reason, the smoother is used to reduce additive broad-band noise in all components of the 3-D data, prior to the rigid body calculations.

The orientation and location of each BFCS is determined by comparing the calculated

LED positions to the segment file information. Orientation quaternions are determined using Schut's algorithm [19], employing a least-squares solution. The positions of the BFCS origins are calculated by matching the centroid of the LEDs on an array and the centroid of the corresponding segment file LEDs.

To obtain linear and angular velocities, the BFCS data are differentiated, using a simple finite differences algorithm. A three-point filter was chosen for its favorable frequency characteristics, and because a minimal impulse response length was desired.

4.2 Data Smoothing

In the TRACK software, a spline smoothing algorithm developed by Dohrmann [4, 5] is used. A time-domain approach was preferred over a filter, since neither the frequency content of the signal nor the characteristics of the noise are known *a priori*. Smoothing has also been shown to yield signal-to-noise ratios superior to those obtained from filtering [14, 16].

Dohrmann's algorithm uses dynamic programming techniques to find the polynomial spline function $f(t)$ which minimizes the functional

$$\varphi(f) = \sum_{k=1}^{n} (f(t_k) - y_k)^2 / w_k^2 + \beta \int_{t_1}^{t_n} (f^{(m)}(t))^2 dt \tag{4.1}$$

where y_k is the data at time $t = t_k$, w_k a weighting term, and the positive constant β is the *smoothing parameter*. The constant m is the *derivative performance criterion* and can take on the values $1, \ldots, p$, where p is the degree of the spline function.

In contrast to natural splines, for which $p = 2m-1$, the above approach allows p and m to be specified independently. For natural splines, the derivatives of order $m, \ldots, 2m-2$ are required to vanish at the endpoints of the data record; since this restriction may not be appropriate for smoothing of biokinematic data, natural splines were avoided.

The smoothing parameter β is chosen using *generalized cross-validation*. The technique models the data as consisting of a smooth function $g(t)$ and an additive stochastic error ϵ_k:

$$y_k = g(t_k) + \epsilon_k \qquad\qquad k = 1, \ldots, n \tag{4.2}$$

where the error term has expected values

$$E(\epsilon_k) = 0, \tag{4.3}$$

$$E(\epsilon_k\, \epsilon_k) = w_k^2 \sigma^2, \tag{4.4}$$

$$E(\epsilon_k\, \epsilon_l) = 0 \qquad \text{for } k \neq l. \tag{4.5}$$

The minimizer of the generalized cross-validation function $V(\beta)$ yields a near-optimal value for the smoothing parameter (see [4]), and does not require knowledge of σ^2.

In the course of experimenting with the smoothing algorithm, it was discovered that step-like transients in the data may cause undesirable behavior in the smoothed output.

Figure 4.2 shows hypothetical noisy data for which the underlying function $g(t)$ is a constant throughout the data set. The corresponding smoothed data (Fig. 4.3) is a very good approximation to $g(t)$. However, if $g(t)$ is a step function (see Fig. 4.4), the smoothing algorithm yields a less accurate output (Fig. 4.5).

One may conclude that the presence of step-like transients in experimental data can potentially affect the selection of β in an adverse manner. Thus, it is prudent to minimize step-like behavior in the data through processing prior to smoothing. In the TRACK software this may be achieved by selecting appropriate values of the window and the cutoff levels e_{SKEW} and e_{ARRAY}.

4.3 Selection of Processing Parameters

The processing of the data is governed by the selection of the parameters e_{SKEW}, e_{ARRAY}, p, m, and the window boundaries. Since the objective is to maximize smoothness (for good velocity estimates) under the constraints of maintaining fidelity to the measured data, and requiring consistency across different data sets (for comparisons), one must determine an optimal set of processing parameters. An extensive search procedure, outlined below, was conducted.

Evaluation of smoothness was done by visual inspection of data plots. To study the effect of e_{SKEW} and e_{ARRAY}, the data were processed for different combinations

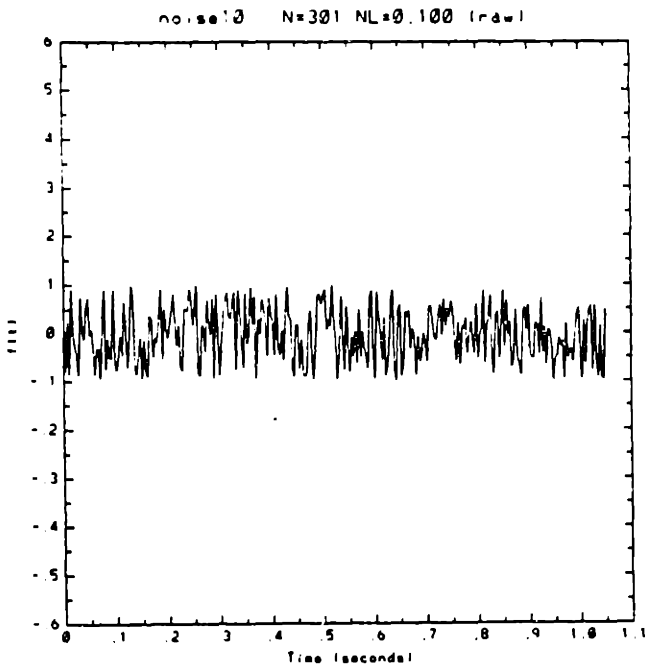

Figure 4.2: Noisy data

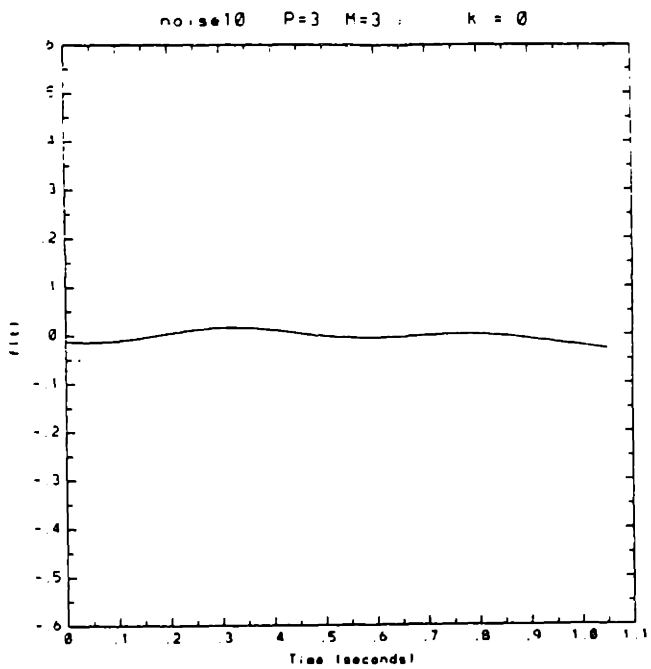

Figure 4.3: Smoothed output

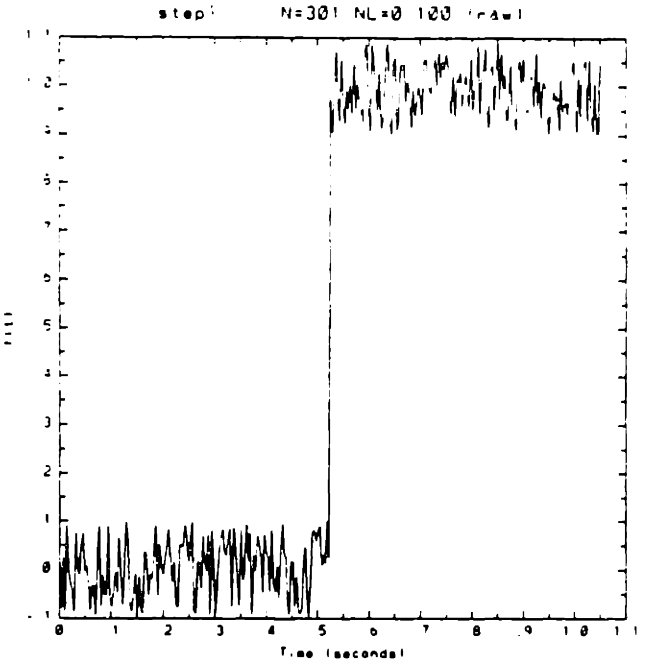

Figure 4.4: Noisy data with step function

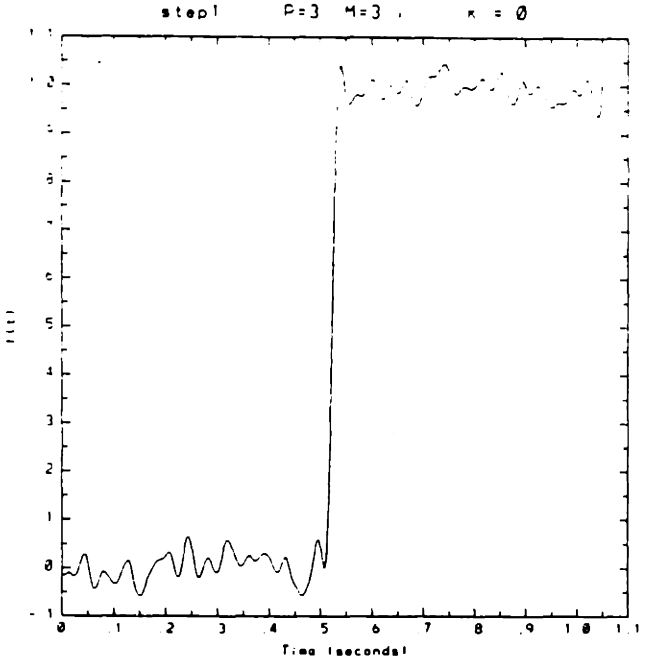

Figure 4.5: Smoothed output

of these parameters. By arranging the resulting plots in an array such that e_{SKEW} is increasing along one dimension and e_{ARRAY} is increasing along the other dimension (see Fig. 4.6), trends could be observed. Such arrangements of plots, hereafter referred to as *test matrices*, were usually generated for all data sets to ensure consistency in parameter selection.

Since windowing and elimination of skew ray and inter-LED errors do not alter any data points, the only step in the processing which can cause infidelity is the smoothing. To ensure that the data were not oversmoothed, and that interpolations in gaps in the data record were realistic, plots of smoothed data were compared to corresponding plots with no smoothing.

To find an optimal set of processing parameters, preliminary investigations were performed first with unsmoothed data, then with smoothing. Subsequently, window boundaries were selected, after which the error cutoff levels were optimized using an iterative search.

Initial investigations with unsmoothed data served to elucidate the effects of varying e_{SKEW} and e_{ARRAY}. Data were processed with no windowing and no smoothing; test matrices were generated for several data sets, with e_{SKEW} and e_{ARRAY} varying over a large range. Results indicate that as e_{SKEW} is raised above approximately 50 S.U. and e_{ARRAY} increased beyond approximately 50 %, further increases in the error cutoff levels have no significant effect. As the cutoff levels were decreased, more data were eliminated from each set; for skew ray error cutoffs below approximately 10 S.U., significant amounts of information were lost from the data. Thus, bounds on e_{SKEW} and e_{ARRAY} were determined. Moreover, it was found that data sets became noisier as either error level was increased. So as a guide for finding optimal cutoff levels, e_{SKEW} and e_{ARRAY} should be lowered as far as possible without eliminating too much data from the records.

Preliminary processing trials with smoothing yielded several interesting results. When large spikes or steps were present in the data, the smoothing algorithm yielded relatively noisy output; this effect had been predicted in earlier numerical experiments (see Sec-

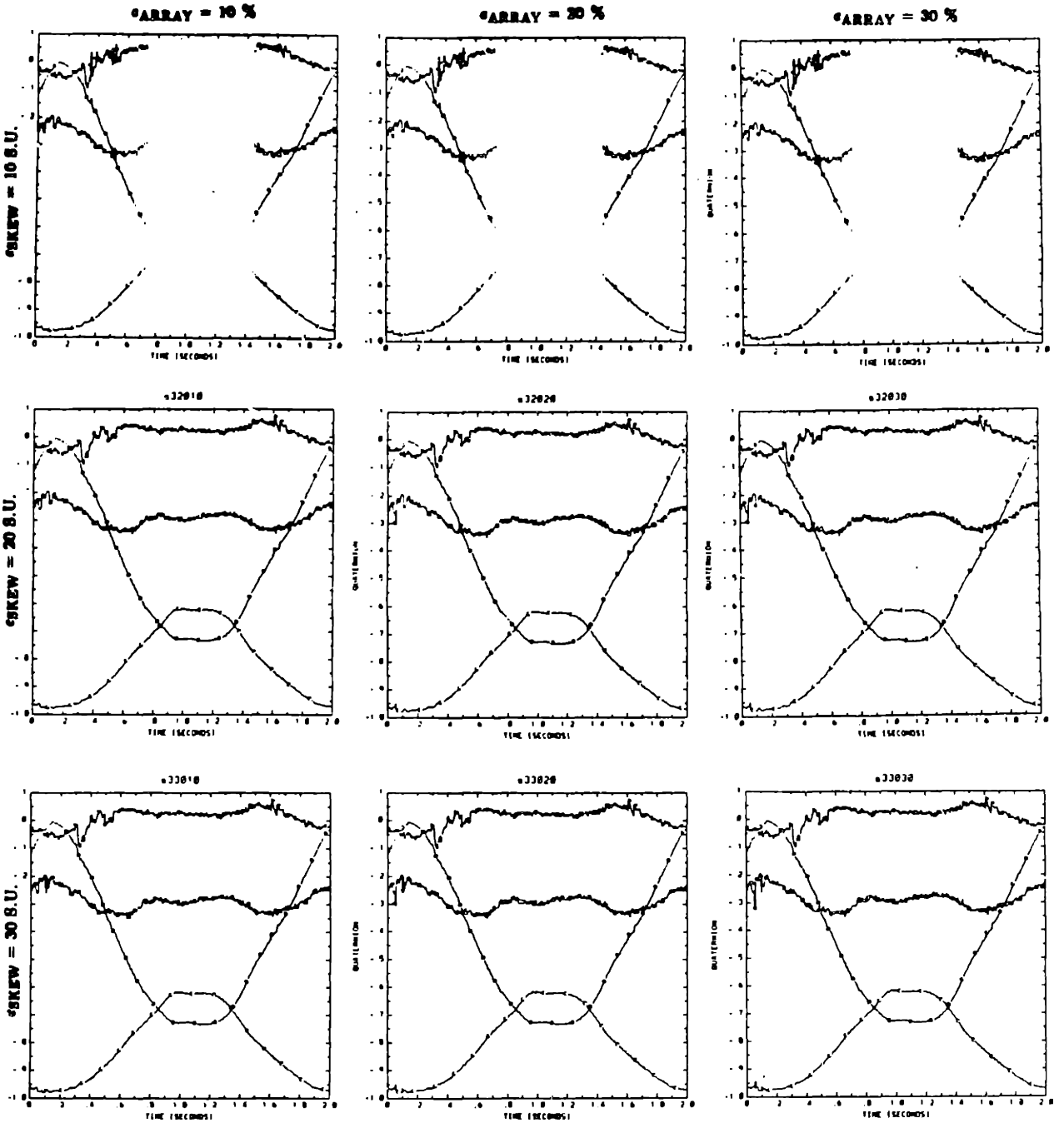

Figure 4.6: Test matrix

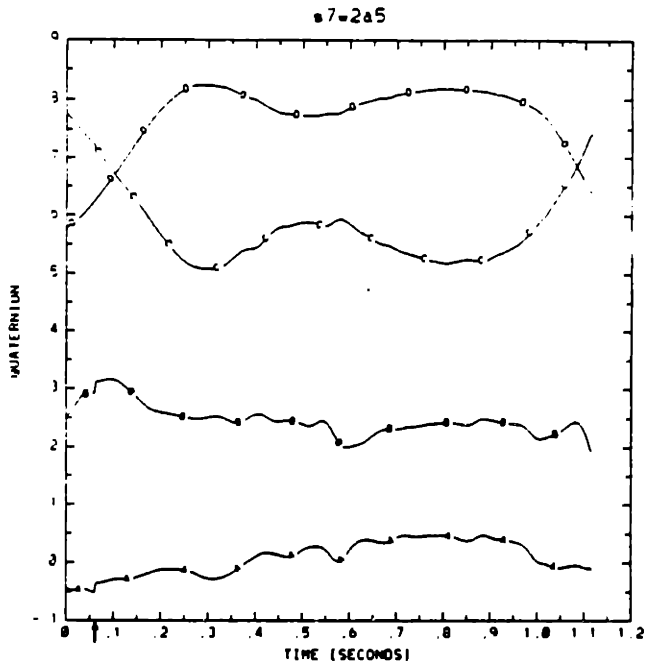

Figure 4.7: Discontinuity in quaternion components at $t \approx 0.06$ s

tion 4.2).

When cubic splines were used, oversmoothing was observed in gait data, especially near heelstrike. This problem could be remedied by using higher order splines.

A final phenomenon observed in the investigations with smoothing was that rigid body calculations from smoothed data yielded discontinuities in some data sets, especially in quaternion components (see Fig. 4.7). This could be explained by the fact that if some LEDs have inadmissible error levels at the beginning or end of an experiment, 3-D data will not be available in those regions for all LEDs on an array. Rigid body data can be obtained as long as at least three LED markers are visible. However, if a redundant LED is included or excluded from the calculations as its error levels cross the threshold values, there is a discrete change in the least-squares solution employed, resulting in a discontinuity in the BFCS data. The size of the discontinuity indicates the magnitude of uncertainty in the solution. By increasing the number of LEDs per array, improved results should be expected. The problem is important, since abrupt changes in the rigid body data will cause poor velocity estimates. However, these difficulties may be circumvented

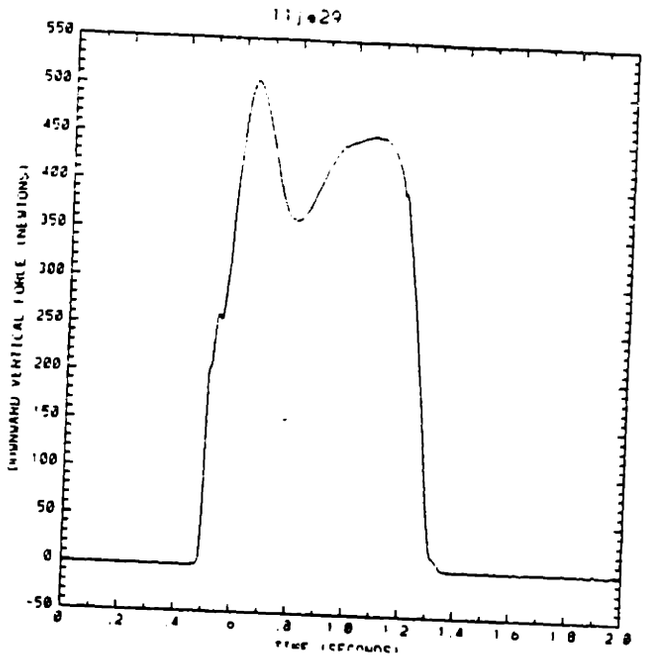

Figure 4.8: Downward force component during gait

through judicious choice of windows, as described below.

Windowing was used to screen out potentially troublesome data at the beginning and end of data sets. Thus window boundaries were chosen so that step- or impulse-like transients were not included, to avoid noisy smoothing; likewise, window endpoints were placed in regions where no LEDs had been eliminated, to avoid discontinuities in BFCS data. Note that gaps inside a window thus defined are filled with interpolated values upon data smoothing, and therefore do not cause discontinuities.

For gait experiments, windowing also served to eliminate unreliable data as the subject entered the field of view of the cameras. With gait data, windows were restricted to include the full stance phase from heelstrike (HS) to toe-off (TO); with swing data, windows were selected to include a flexion-extension cycle. Endpoints of the stance phase were determined from force-plate data; Figure 4.8 shows a representative plot, and results for all gait experiments are summarized in Table 4.1. The chosen window boundaries for all experiments are listed in Table 4.2.

Ideally, all data sets should be processed identically, *i.e.* with the same values of

File	frame		t (s)	
	HS	TO	HS	TO
11JE07	208	434	0.72	1.52
11JE08	224	448	0.78	1.56
11JE09	155	371	0.54	1.30
11JE10	154	386	0.54	1.35
11JE26	91	324	0.32	1.13
11JE27	161	400	0.56	1.40
11JE28	215	448	0.75	1.56
11JE29	137	387	0.48	1.35
11JE30	169	405	0.59	1.41

Table 4.1: Stance phase endpoints for gait experiments

File	frame		t (s)	
	n_1	n_2	t_1	t_2
11JE02	135	532	0.47	1.86
11JE03	167	450	0.58	1.57
11JE04	147	515	0.51	1.80
11JE05	1	571	0.00	2.00
11JE07	110	438	0.38	1.53
11JE08	121	454	0.42	1.59
11JE09	80	393	0.28	1.37
11JE10	115	407	0.40	1.42
11JE21	15	515	0.05	1.80
11JE22	1	508	0.00	1.78
11JE23	1	432	0.00	1.51
11JE24	1	571	0.00	2.00
11JE26	35	330	0.12	1.15
11JE27	75	416	0.26	1.45
11JE28	129	459	0.45	1.60
11JE29	87	415	0.30	1.45
11JE30	87	420	0.30	1.47

Table 4.2: Window boundaries

e_{SKEW}, e_{ARRAY}, p and m. However, trial runs with smoothing indicated that gait data suffered from oversmoothing when $p = 3$ $m = 3$ was used. Accurate smoothing of gait data was obtained for $p = 5$ $m = 5$, but this processing applied to swing data yielded inferior smoothness. Since neither fidelity nor smoothness could be compromised, it was decided to choose a different set of optimal smoothing parameters for gait and swing experiments. The drawback of this is that caution must be used when comparing swing data with gait data, since consistency may be a problem. However, in this work the primary objective is to compare gait experiments to each other and swing experiments to each other, in order to detect differences due to array mounting methods.

To determine the optimal cutoff levels e_{SKEW} and e_{ARRAY} for swing data, an iterative procedure was used. The data were windowed prior to processing, and smoothing was selected with $p = 3$ $m = 3$. Test matrices were run for every swing experiment, and the smoothness of every combination of e_{SKEW} and e_{ARRAY} was evaluated by visual inspection of the plots; the best results were achieved with $e_{SKEW} = 20$ S.U. and $e_{ARRAY} = 5\%$. The fidelity of the data thus processed was evaluated by comparing plots of 3-D data before and after smoothing. Subsequently, each data set was rated on the basis of fidelity and smoothness; a data set with poor interpolations, oversmoothing, or excessive noise was given a low rating, and one with no such problems a high rating. Tables 4.3 and 4.4 list the results for swing data in order of highest to lowest ranking. Since data with a low ranking was not likely to yield any useful results, the test matrices were re-evaluated, this time considering only data sets with high ratings when selecting optimal error cutoff levels. For swing data, $e_{SKEW} = 20$ S.U. and $e_{ARRAY} = 5\%$ again resulted in the smoothest output.

The same procedure detailed above was repeated for gait data, the only difference being that smoothing parameters were $p = 5$ $m = 5$. Ratings were based on stance phase results only. Optimal error cutoffs were $e_{SKEW} = 20$ S.U. and $e_{ARRAY} = 8\%$. Gait data are ranked by smoothness/accuracy ratings in Tables 4.5 and 4.6. Table 4.7 summarizes the optimal processing parameters for both swing and gait data.

File	Rating
11JE03	High
11JE02	High
11JE05	Medium
11JE04	Low

Table 4.3: Ranked Type 1 swing experiments

File	Rating
11JE23	High
11JE24	High
11JE22	Medium
11JE21	Low

Table 4.4: Ranked Type 2 swing experiments

File	Rating
11JE10	High
11JE07	High
11JE08	Low
11JE09	Low

Table 4.5: Ranked Type 1 gait experiments

File	Rating
11JE29	High
11JE30	High
11JE28	High
11JE26	High
11JE27	High

Table 4.6: Ranked Type 2 gait experiments

Task	p	m	e_{SKEW}	e_{ARRAY}
Swing	3	3	20	5 %
Gait	5	5	20	8 %

Table 4.7: Optimal processing parameters

File	frame		t (s)	
	n_1	n_2	t_1	t_2
11JE02	144	508	0.50	1.78
11JE05	241	487	0.84	1.70
11JE07	24	329	0.08	1.15
11JE10	1	293	0.00	1.02
11JE23	1	419	0.00	1.46
11JE26	44	296	0.15	1.03
11JE27	58	342	0.20	1.20
11JE28	58	331	0.20	1.16
11JE29	1	329	0.00	1.15
11JE30	44	334	0.15	1.17

Table 4.8: Post-TRACK windows

4.4 Post-TRACK Procesing

Since fidelity in processed gait data was evaluated in the stance phase only, a given data set may contain regions of inaccuracy. Similarly for swing experiments, two of the data sets which received low ratings showed poor fidelity only in localized sections. By windowing these data after TRACK processing, the accurate sections of the swing data can be salvaged, and the gait data can be screened to ensure that no corrupt data are used in further calculations. The post-TRACK window boundaries are listed in Table 4.8.

The TRACK procesing software calculates $\mathbf{x_{01}}$, q_{01}, $\dot{\mathbf{x}}_{\mathbf{01}}$, and $\dot{q}_{01}$ describing the motion of the BFCS associated with the femoral array, and $\mathbf{x_{02}}$, q_{02}, $\dot{\mathbf{x}}_{\mathbf{02}}$, and $\dot{q}_{02}$ corresponding to the tibial BFCS. These values were used to calculate the instantaneous helical axes, as described in Section 3.3.

Chapter 5

Error Analysis

Figure 5.1 illustrates the relationship between the measured kinematics and the actual skeletal motion. The target motion (a) is the time history of the position and orientation of a coordinate system fixed with respect to the bone; this is the desired information for joint analysis. However, the body-fixed coordinate systems are defined with respect to the marker arrays. Thus, if the array is not directly affixed to the bone, the target BFCS and the array BFCS (b) will be distinct. Moreover, since no camera system is ideal, the perceived array image (c) will be different from the actual array, with a corresponding discrepancy in BFCS data.

The objectives of this work are to detect any differences between target motion and array motion, for two different array mounting schemes, and to determine whether system noise prohibits the use of IHA methods for comparing data.

Measurement errors or noise will manifest themselves in the form of discrepancies between the array and its image. There are many sources of error; here, the effect of stochastic errors only will be studied.

Stochastic errors in the data are due to noise in the electronic components of the data acquisition system, as well as discretization errors in the A/D conversion. Mansfield has shown that the stochastic noise in the data is correlated with the LED intensity [2]. Thus, the further away the TRACK array is from the cameras, and the more the array faces away from a camera, the higher the standard deviation of the stochastic noise.

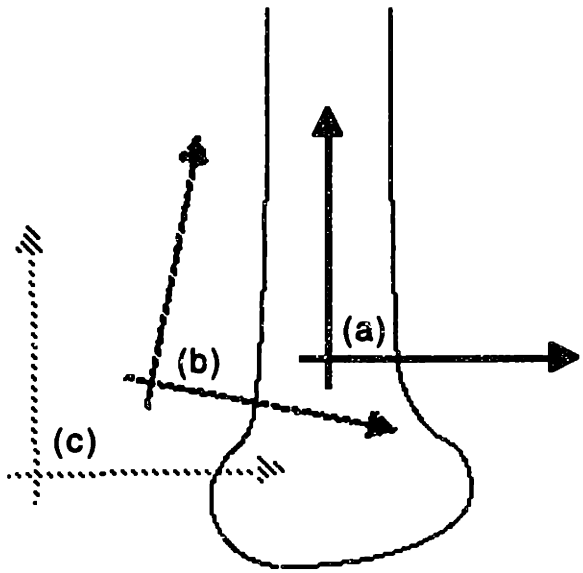

Figure 5.1: (a) Target BFCS (b) Array BFCS (c) Image BFCS

In addition to random errors, there is a presence of systematic errors. These are due to errors in system calibration, as well as camera nonlinearities.

A final source of measurement error is reflections. Since the Selspot II cameras output the coordinates of the center of intensity of all light striking the detector plate, LED position measurements are distorted if there are reflections in the field of view of the cameras. Errors of this type are virtually impossible to model or detect, and thus present some problem in data analysis.

The TRACK data processing software (see Section 4.1) can be used to reduce the effect of measurement errors. Reflections and systematic errors in the data would give rise to increased skew ray and inter-LED errors; by choosing appropriate values for e_{SKEW} and e_{ARRAY}, corrupt data can be eliminated. Stochastic noise can be reduced by smoothing the data.

To study the effect of random errors on the IHA calculation, static experiments were analyzed. In static trials, the subject was standing motionless; thus the error component is expected to be dominated by stochastic noise. To verify this, the standard deviations of

Standard deviation	x (mm)	y (mm)	z(mm)
Predicted	0.14	0.14	0.41
Type 1 mounting	0.15	0.10	0.24
Type 2 mounting	0.07	0.22	0.19

Table 5.1: Predicted and empirical standard deviations in position vector

$\mathbf{x_{01}}$ and $\mathbf{x_{02}}$, the positions of the femoral and tibial BFCSs were calculated for each static experiment. These numbers were compared to the corresponding predicted standard deviations which would result from a variation of $\pm$ 1 S.U. in the measurements. This is the magnitude of the discretization error, and it is also on the order of the magnitude of the stochastic error for the brightest LED intensity. The predicted standard deviations agree well with the empirical static deviations (see Table 5.1).

The static experiments appear to be good indicators of the amount of random errors in the measured data. Thus, to estimate the effect of stochastic noise on velocity calculations, static data were differentiated. Since the premise of a static experiment is that there is virtually no motion, verified by the data in Table 5.1, any non-zero velocity component was interpreted as an error. The static data sets were processed the same way as gait and free swing data (see Table 4.7). Linear and angular velocities of the tibial BFCS with respect to the femoral BFCS were calculated and graphed (see Figures 5.2 - 5.9). Error levels were assessed visually; results are listed in Table 5.2. These are estimated lower bounds of the velocity errors, since dynamic effects have been neglected.

The z-component of the angular velocity error is consistently lower in magnitude than the corresponding x- and y-components; similarly, the z-component of the error in linear velocity is of greater magnitude than the errors in x and y. This can be explained by the larger variation in the z-component of the position vector (see Table 5.1), which in turn is a result of camera orientations. Upon differentiation, higher noise levels in the z-coordinate will cause correspondingly higher error levels in the z-component of the linear velocity. Angular velocity estimates in the x- and y-directions would be adversely

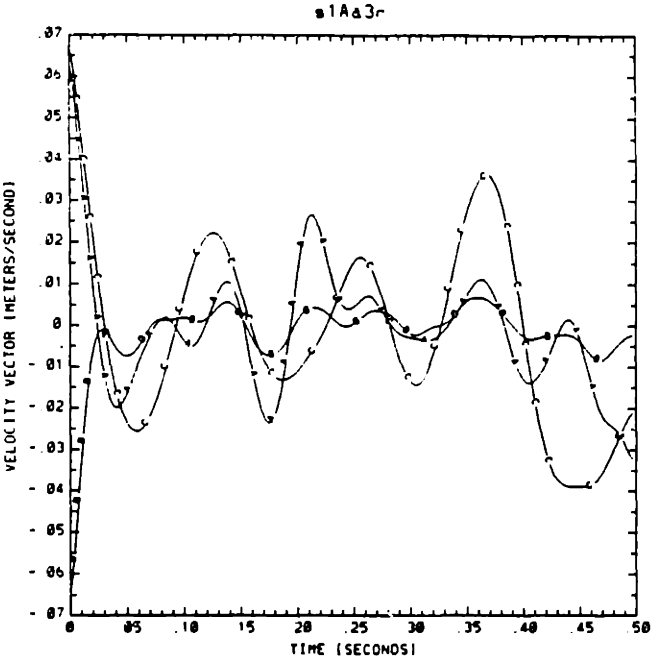

Figure 5.2: Static trial linear velocity for Type 1 mounting, processed like swing data

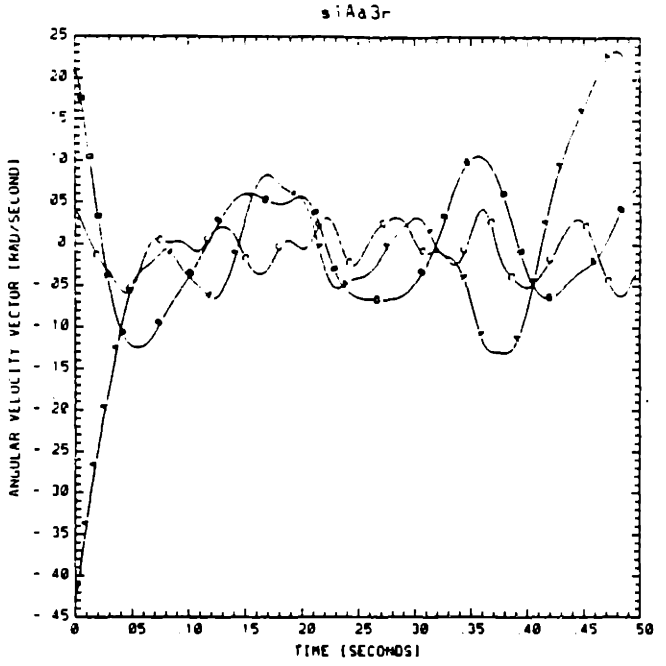

Figure 5.3: Static trial angular velocity for Type 1 mounting, processed like swing data

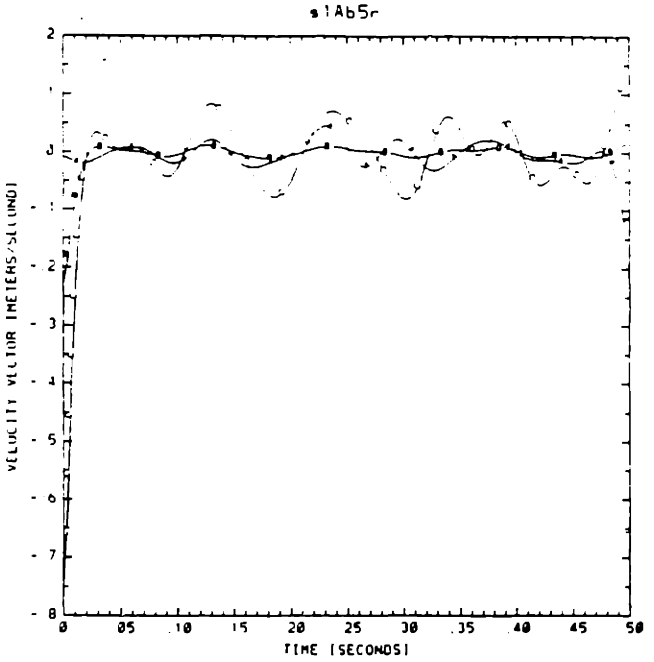

Figure 5.4: Static trial linear velocity for Type 1 mounting, processed like gait data

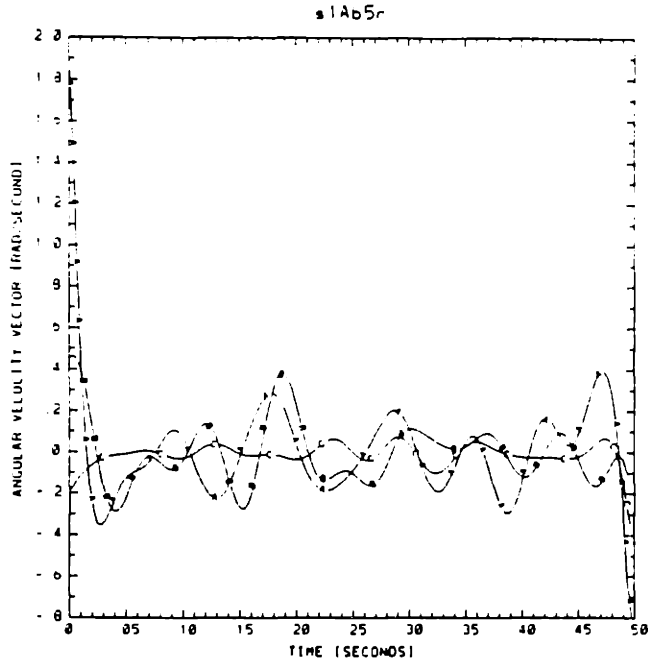

Figure 5.5: Static trial angular velocity for Type 1 mounting, processed like gait data

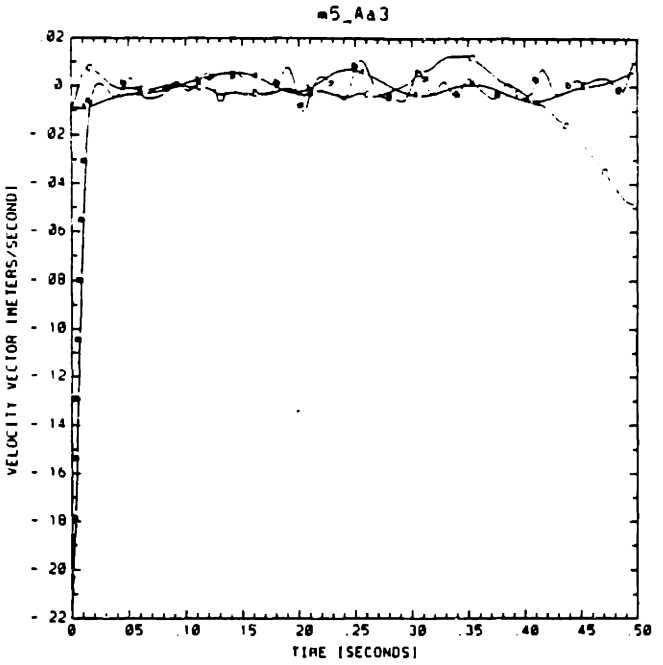

Figure 5.6: Static trial linear velocity for Type 2 mounting, processed like swing data

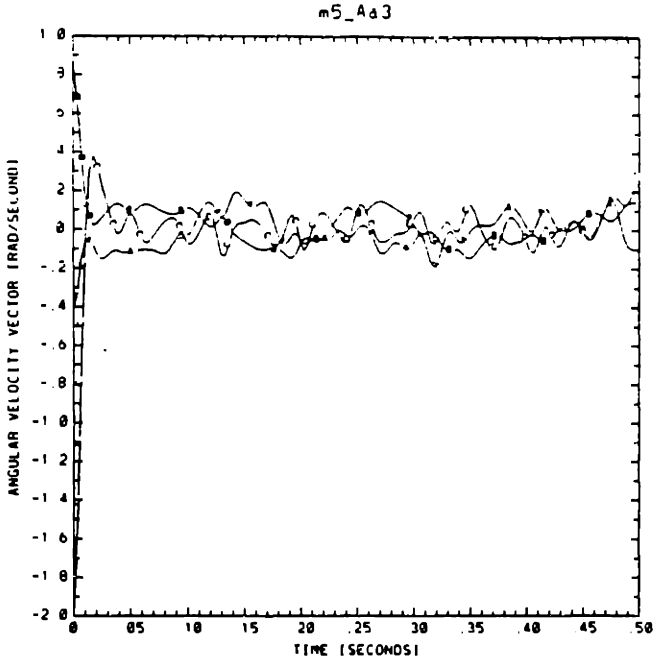

Figure 5.7: Static trial angular velocity for Type 2 mounting, processed like swing data

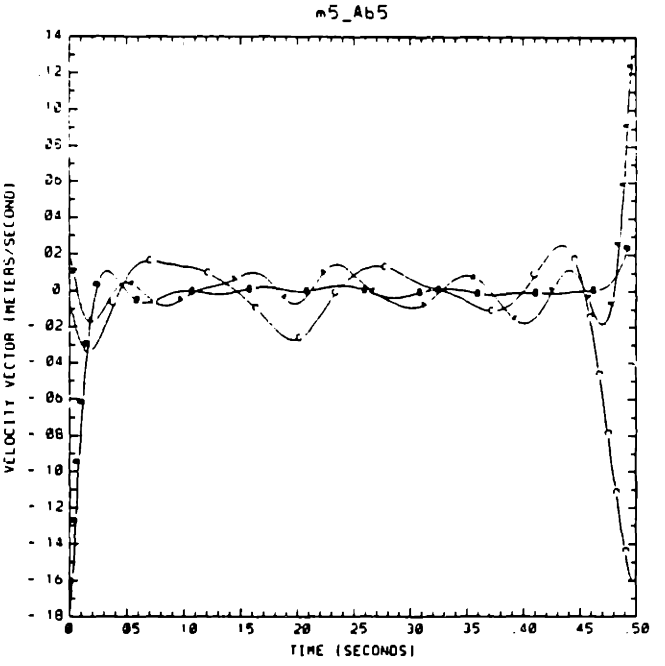

Figure 5.8: Static trial linear velocity for Type 2 mounting, processed like gait data

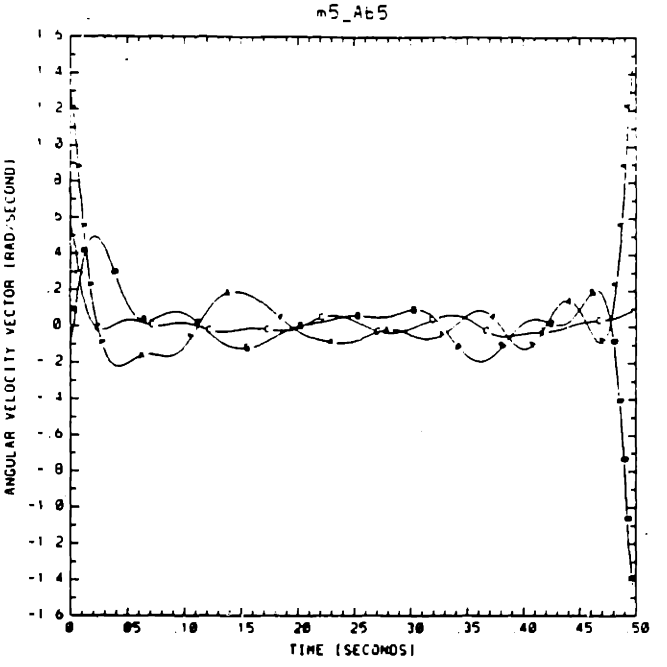

Figure 5.9: Static trial angular velocity for Type 2 mounting, processed like gait data

Task	Swing		Gait	
Mounting	Type 1	Type 2	Type 1	Type 2
$\delta\Omega_x$ (rad/s)	0.13	0.1	0.22	0.15
$\delta\Omega_y$ (rad/s)	0.1	0.1	0.17	0.15
$\delta\Omega_z$ (rad/s)	0.04	0.08	0.06	0.05
δv_x (m/s)	0.015	0.006	0.03	0.01
δv_y (m/s)	0.005	0.006	0.01	0.004
δv_z (m/s)	0.028	0.015	0.06	0.015

Table 5.2: Estimated error levels

affected as well.

5.1 Compounding of Errors

A set of stochastic errors dx_i in corresponding independent variables x_i, $i = 1, \ldots, n$, will propagate to yield an average deviation δy in a derived quantity y,

$$y = F(x_1, \ldots, x_n). \tag{5.1}$$

If the expectation values of the errors dx_i satisfy

$$E(dx_i) = 0, \tag{5.2}$$

$$E(dx_i^2) = \delta x_i^2, \tag{5.3}$$

$$E(dx_i\, dx_j) = 0 \qquad \text{for } i \neq j, \tag{5.4}$$

and δx_i is small, then

$$\delta y = \sum_{i=1}^{n} \left(\frac{\partial F}{\partial x_i}\right)^2 \delta x_i^2. \tag{5.5}$$

The IHA components $\mathbf{r}$ and $\mathbf{p}$ are functions of $\mathbf{x}$, $\mathbf{v}$ and Ω (see Section 3.3). Although these variables are not truly independent, Equation 5.5 is used here to estimate the error levels $\delta\mathbf{r}$ and $\delta\mathbf{p}$.

Since the partial derivatives $\frac{\partial F}{\partial x_i}$ depend on the instantaneous values of $\mathbf{x}$, $\mathbf{v}$ and Ω, the compounded errors $\delta\mathbf{r}$ and $\delta\mathbf{p}$ were evaluated for each Selspot frame. By studying plots

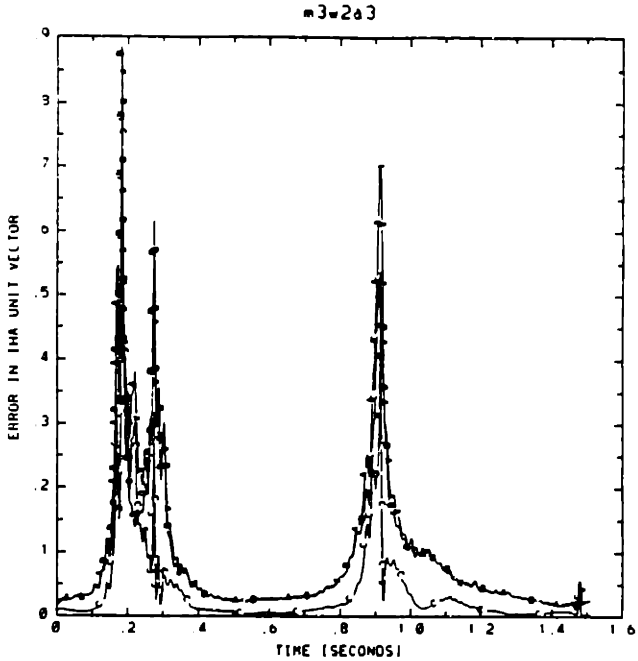

Figure 5.10: Error levels during free swing experiment

of $\delta\mathbf{r}$ and $\delta\mathbf{p}$ as functions of time, error magnitudes can be estimated for different phases of an experiment. A plot of a free swing experiment shows that at terminal extension and flexion, error levels increase dramatically (see Fig. 5.10). This happens because as the subject reaches the limits of the range of motion and reverses the direction of swing, the angular velocity approaches zero magnitude, resulting in unreliable estimates of the IHA direction and location.

In order to screen out IHA data with excessive error levels, plots of $\delta\mathbf{r}$ versus angular speed were generated (see Figure 5.11). As expected, error magnitudes increase rapidly for low angular speeds. By choosing a cutoff level for the magnitude of the angular velocity vector, data with slow speeds, and thus large errors, can be excluded. Angular speed thresholds were selected such that the error in any component of $\mathbf{r}$ did not exceed 0.1. Results are shown in Table 5.3.

Data which have been screened as described above will have errors in unit vector components on the order of

$$\delta r_x \approx \delta r_y \approx \delta r_z \approx 0.1.$$

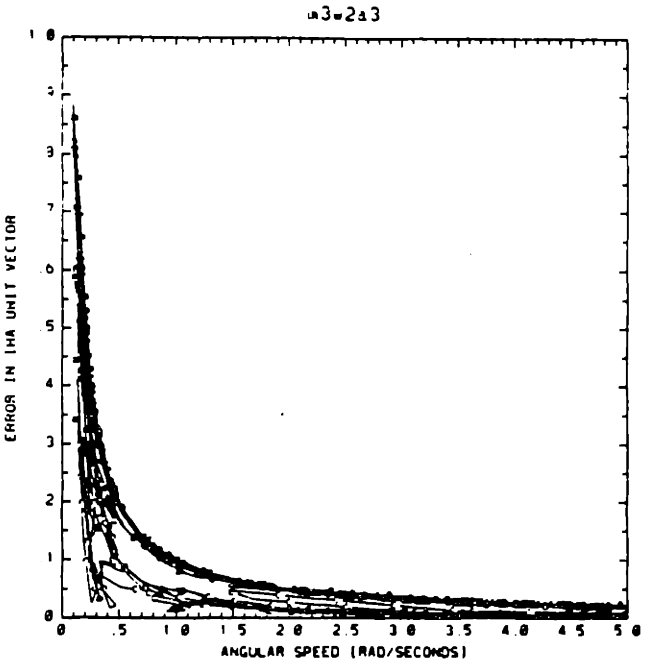

Figure 5.11: Error levels versus angular speed

Task	Mounting	Cutoff (rad/s)
Swing	Type 1	1.2
	Type 2	1.0
Gait	Type 1	1.3
	Type 2	1.5

Table 5.3: Angular speed threshold levels

Task	Mounting	Error		
		δp_x (m)	δp_y (m)	δp_z (m)
Swing	Type 1	0.010	0.020	0.030
	Type 2	0.025	0.025	0.025
Gait	Type 1	0.020	0.020	0.020
	Type 2	0.010	0.020	0.020

Table 5.4: Error levels in IHA location

By graphing δ**p** versus angular speed, and determining the approximate error levels corresponding to the threshold angular speed (see Table 5.3), deviations in the IHA position vector components were estimated. Results are shown in Table 5.4.

These error levels are estimated lower bounds on the actual variations in the IHA components **r** and **p** due to stochastic noise. They indicate the order of magnitude of the accuracy of the IHA calculations.

Chapter 6

Results and Discussion

Data from the experiments with skin-mounted marker arrays were processed as described in Chapter 4, and screened for low angular speeds as outlined in Section 5.1. Instantaneous helical axes were determined using the formulas in Section 3.3. The femoral array BFCS was chosen as the reference frame for representations of the relative kinematics. The location and orientation of the BFCSs with respect to the corresponding arrays are defined in the segment file for each mounting type (see Section 4.1). By redefining the femoral BFCS so that its average orientation in the static trial coincided with the global laboratory frame orientation, a fairly consistent reference is obtained for comparing orientation of specific elements of the axodes obtained in different experiments. This procedure yielded a BFCS orientation with respect to the femur as shown in Figure 6.1: the y-axis is approximately aligned with the long axis of the femur, the x-axis is in the anterior-posterior direction, and the z-axis in the lateral-medial direction. There will be some variation in the reference BFCS definitions corresponding to the different mounting methods, due to the fact that the femur of the subject did not have exactly the same orientation in the static experiments for each mounting type. However, it is reasonable to assume that this variation is at most on the order of 5-10 degrees rotational bias. Thus, axode orientations may be compared; to avoid any problems related to discrepancies in BFCS orientations, however, comparison should be restricted to the shape of the axodes.

In the comparative analyses presented below, attention is focussed on the behavior of

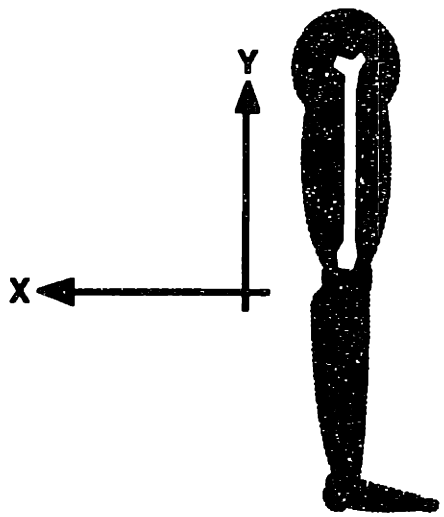

Figure 6.1: Orientation of femur in reference BFCS

the unit vector representing IHA direction. This is because the errors in the components of the IHA location vector are on the order of the physical dimensions of the knee joint, and often on the order of variations in the location vector (see Section 5.1); thus, little or no insight is gained from IHA location data.

Results from the study using bone-pins are presented for reference. For a description of the processing of these data, and a detailed analysis of the results, see Murphy, 1990 [13].

A comparison of axodes representing kinematic data measured using arrays mounted on pins, and with Type 1 and Type 2 mounting follows. Results from voluntary swing and gait trials are included; the data shown are representative of the various trials for each combination of task and attachment method.

6.1 Voluntary Swing

Figures 6.2 and 6.3 show the IHA direction and location as functions of time for a swing experiment with pin-mounted arrays. Figure 6.4 has the corresponding axode plotted as a three-dimensional ruled suface. The observed gaps in the graphs correspond to data

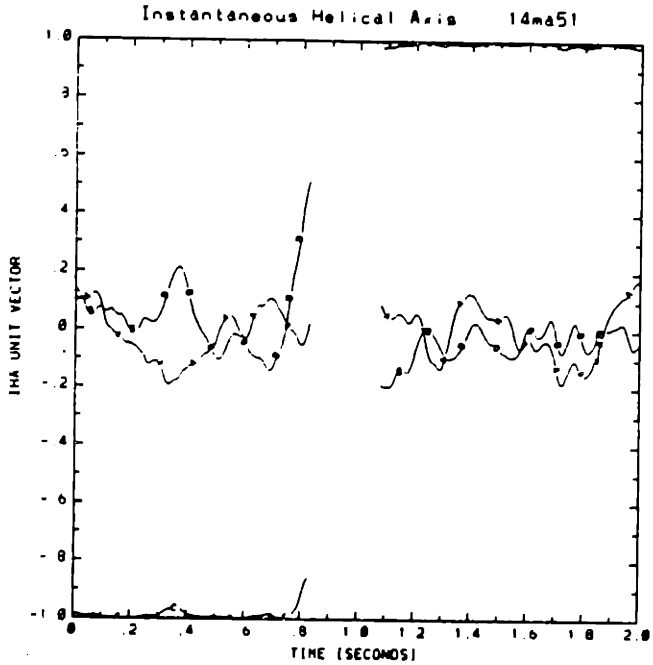

Figure 6.2: IHA direction for swing, Trial 2 with pin mounting

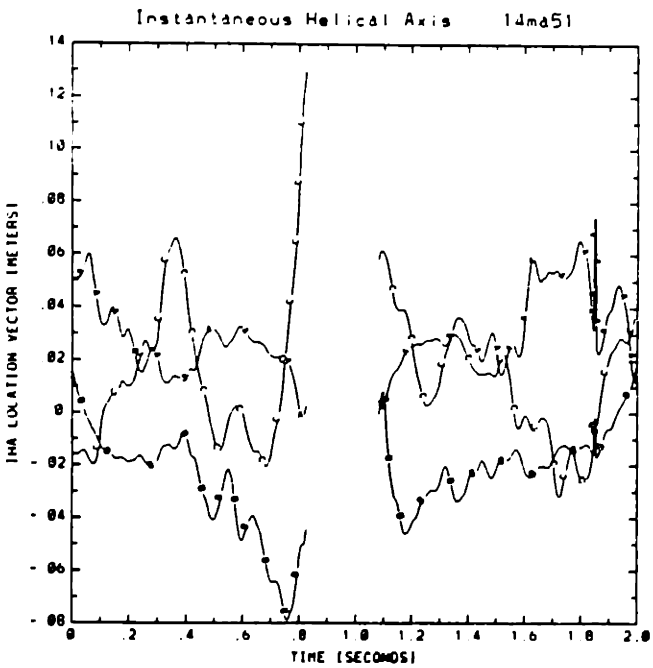

Figure 6.3: IHA location for swing, Trial 2 with pin mounting

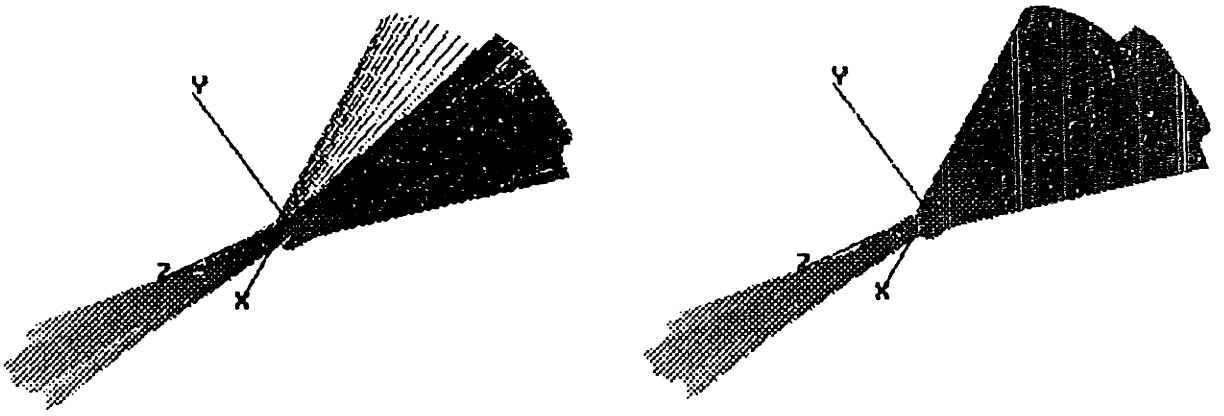

Figure 6.4: Axode for swing, Trial 2 with pin mounting

eliminated because the angular speed was too low (see Section 5.1).

The motion starts out with an extension (dominant rotation component is in the negative z-direction); the reversal in IHA direction to a predominantly positive z-rotation indicates flexion.

As can be seen, the IHA direction stays very constant during both flexion and extension. The fluctuations seen in the x- and y-components of the unit vector are approximately on the order of the estimated errors due to stochastic noise. Thus the motion of the tibia relative to the femur appears to be very close to planar for voluntary swing tasks. The axode is practically parallel to the z-axis of the femoral BFCS.

Swing data from external mounting Type 1 are shown in Figures 6.5, 6.6, and 6.7. The gross features of the axode are similar to those for the pin data: extension is marked by a cluster of IHAs with large negative z-components, flexion by an IHA cluster in the opposite direction. A more careful examination, however, reveals some differences between pin and Type 1 mounting. The dominant axode direction appears to have an orientation which is offset from the almost pure z-rotation seen in the pin data. Also,

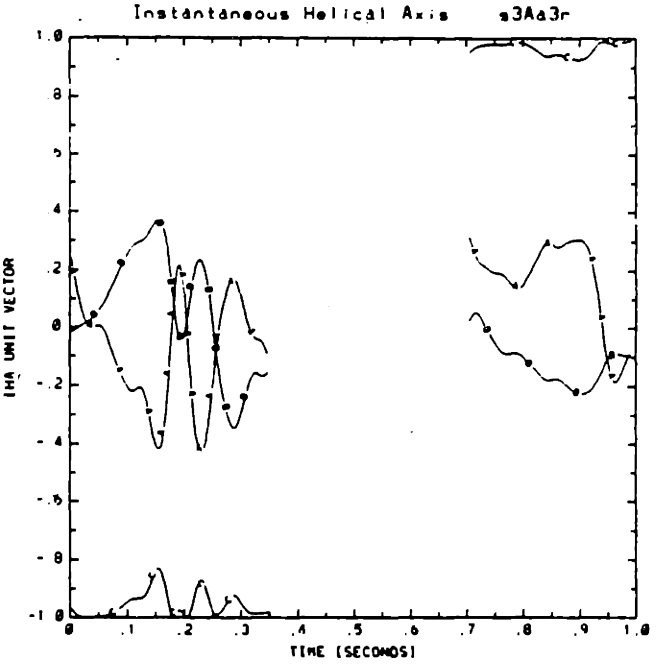

Figure 6.5: IHA direction for swing, Trial 2 with Type 1 mounting

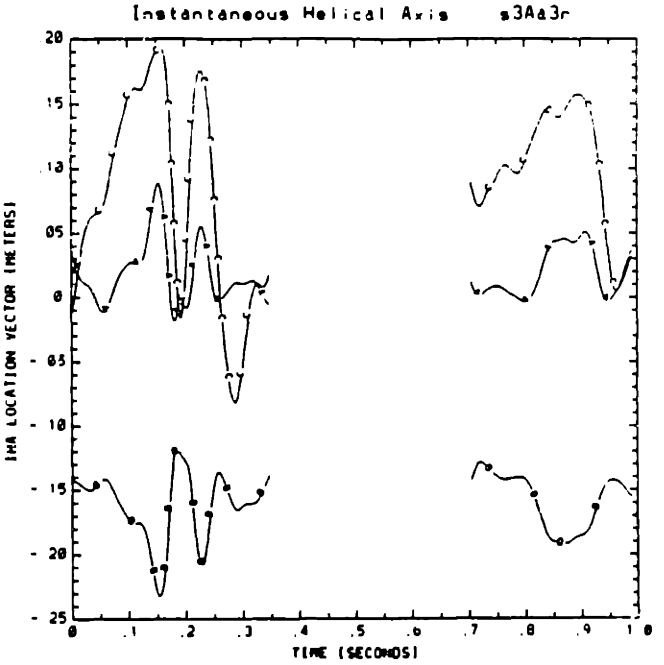

Figure 6.6: IHA location for swing, Trial 2 with Type 1 mounting

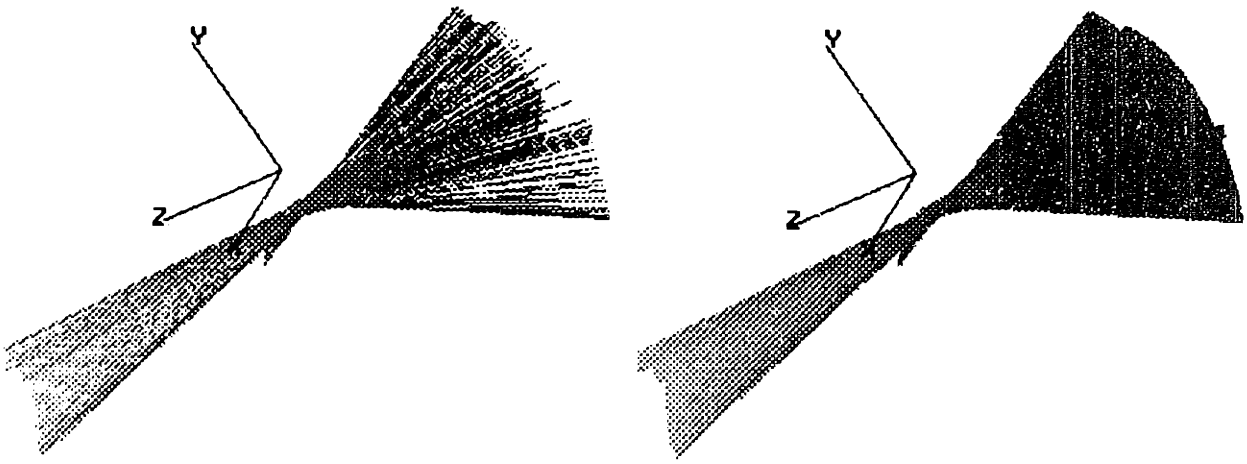

Figure 6.7: Axode for swing, Trial 2 with Type 1 mounting

variations in the x- and y-components of the IHA unit vector are significant compared to the estimated error of 0.1 (see Section 5.1). The effect of these variations is to cause cone-like structures in the axode.

This particular trial showed a significant deviation in the IHA components at $t \approx 0.15$ s (see Fig. 6.5). However, an examination of the 3-D position data of the individual LED markers yields evidence of a distortion due to reflections. Figure 6.8 shows the z-component of the tibial markers, measured in the laboratory frame. The gap at $t \approx 0.15$ s - 0.20 s in the data from marker C indicates that skew ray and/or inter-LED errors are high. Also significant, a concurrent, sudden jump in the trajectory of marker D, is not accompanied by correlated motion in the other markers, as would be expected if the spike corresponded to a real array motion. These observation suggest that the apparent fluctuation in IHA components at around $t \approx 0.15$ s is due to measurement errors. IHA variations in the remainder of the data record, however, appear to be caused by actual array motion.

Data from a swing trial with Type 2 mounting, shown in Figures 6.9, 6.10 and 6.11,

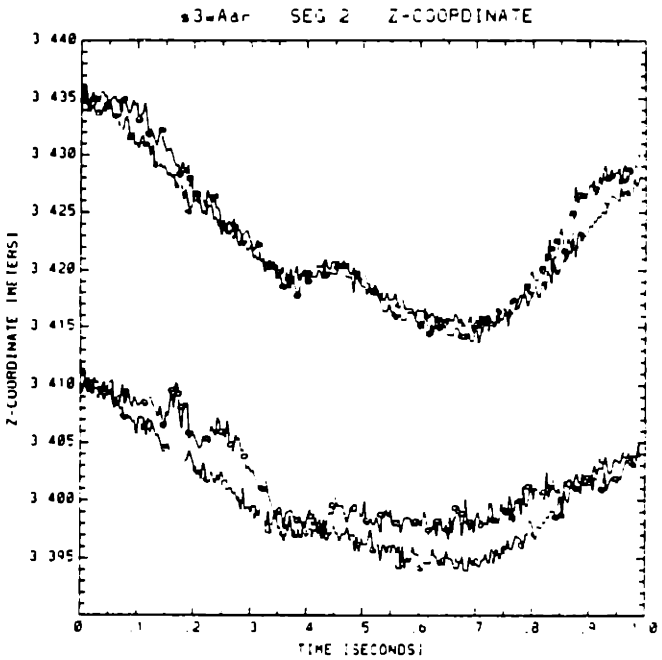

Figure 6.8: Position data for tibial array LEDs

is similar to Type 1 data. The primary IHA direction deviates from the z-axis, and fluctuations in the axode about this direction have significant magnitude compared with estimated noise levels. In Figure 6.11, the resulting conical structure in the axode can be seen; the fine-scale random variations superimposed on this structure are due to stochastic errors.

Comparing the data from the three mounting methods, the following observations can be made. All experiments reveal the basic extension-flexion motion; the pin data indicates that the mechanism is very planar,having IHAs closely aligned with the z-axis. Both external mounting methods yield similar results, differing from the pin data in the orientation and the shape of the axode.

For skin-mounted arrays, the primary direction of the axodes has a significant y-component and a slight x-component. This apparent rotation of the axode relative to the pin data axode may be due to one of the following reasons: (1) difference in orientation of the femur with respect to the laboratory frame in the static experiments for direct and external mounting; (2) difference in underlying mechanism between the pin

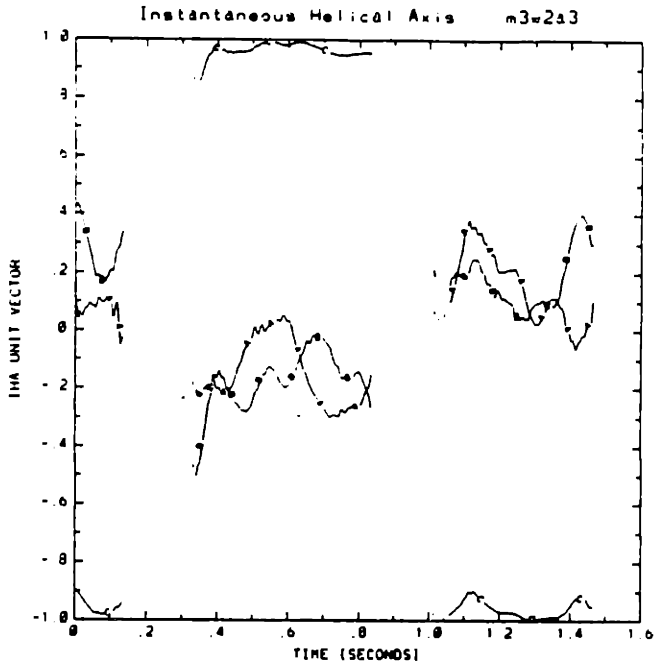

Figure 6.9: IHA direction for swing, Trial 3 with Type 2 mounting

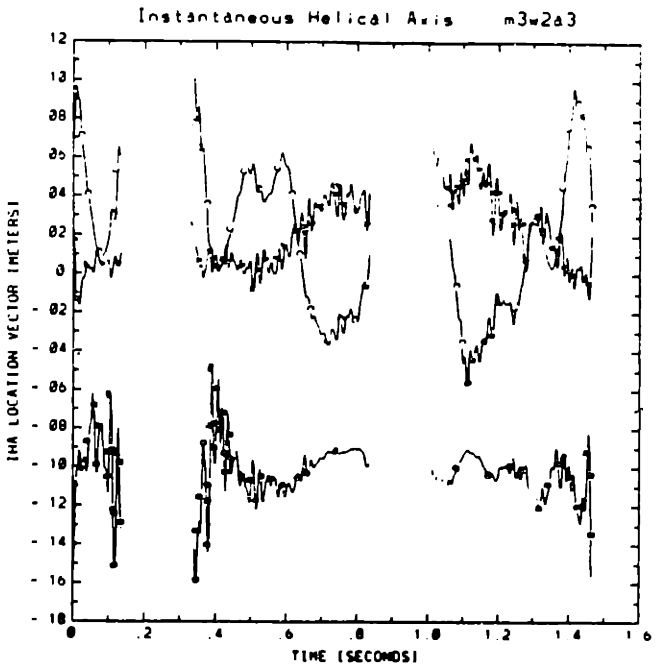

Figure 6.10: IHA location for swing, Trial 3 with Type 2 mounting

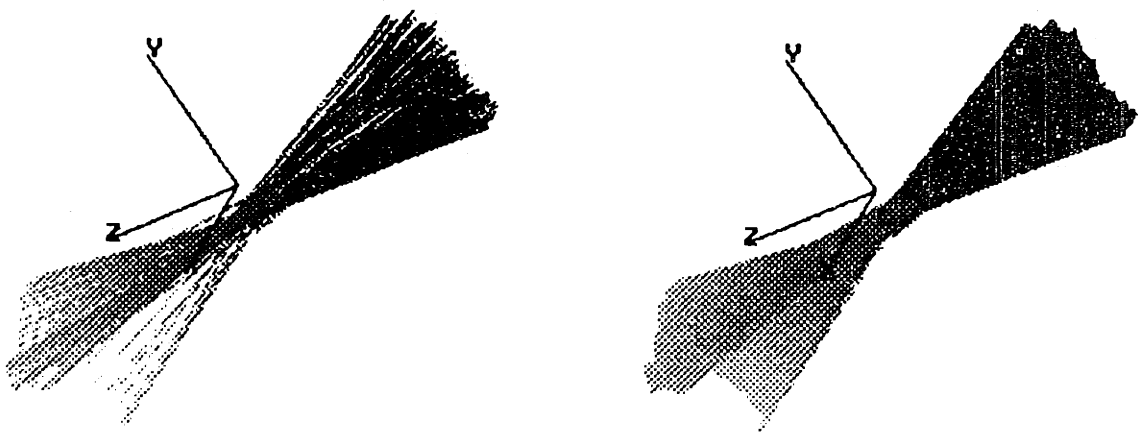

Figure 6.11: Axode for swing, Trial 3 with Type 2 mounting

experiments and the experiments with external markers, which were conducted one year apart; (3) artifactual soft tissue motion in external marker data.

Comparing just the shapes of the axodes, thus avoiding problems associated with inconsistent BFCS definitions, it is seen that skin-mounted markers yield axodes having a cone-like structure, in contrast to the pin data IHAs, which stay largely in the same direction. Thus, while the directly measured kinematics indicate a planar mechanism for swing, externally mounted arrays measure a three-dimensional motion. Since the deviations from planar kinematics are significant with respect to estimated error magnitudes, one may attribute the observed out-of-plane motion to soft tissue movement.

6.2 Gait

Figures 6.12 and 6.13 show IHA components for gait data from bone-mounted arrays. The corresponding axode, shown in Figure 6.14, indicates a mechanism which differs from that seen for voluntary swing. Four main structures can be identified; they are: (1) initial

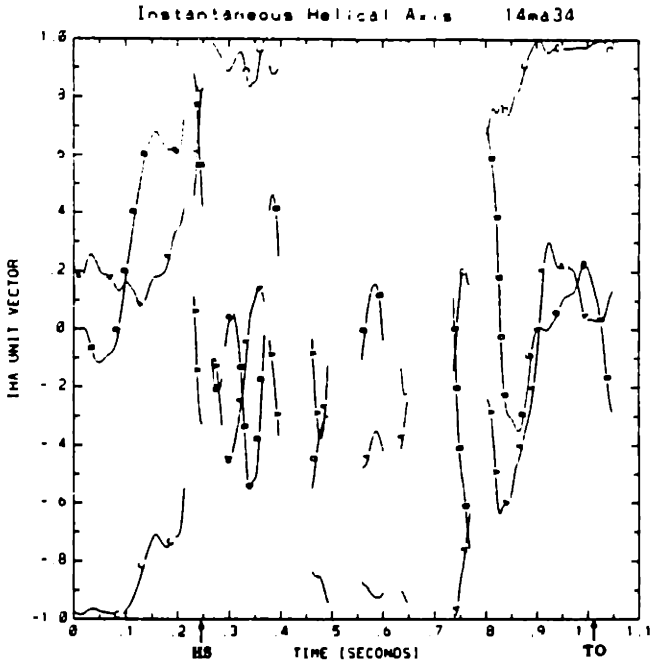

Figure 6.12: IHA direction for gait, Trial 1 with pin mounting

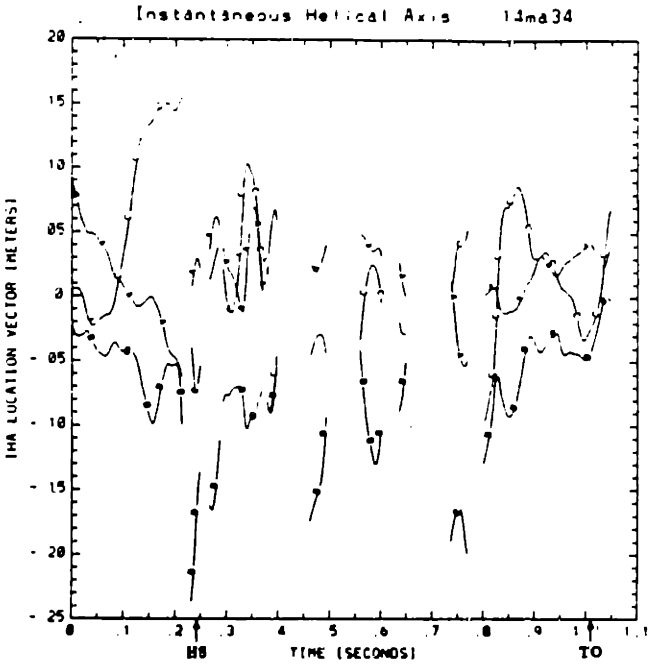

Figure 6.13: IHA location for gait, Trial 1 with pin mounting

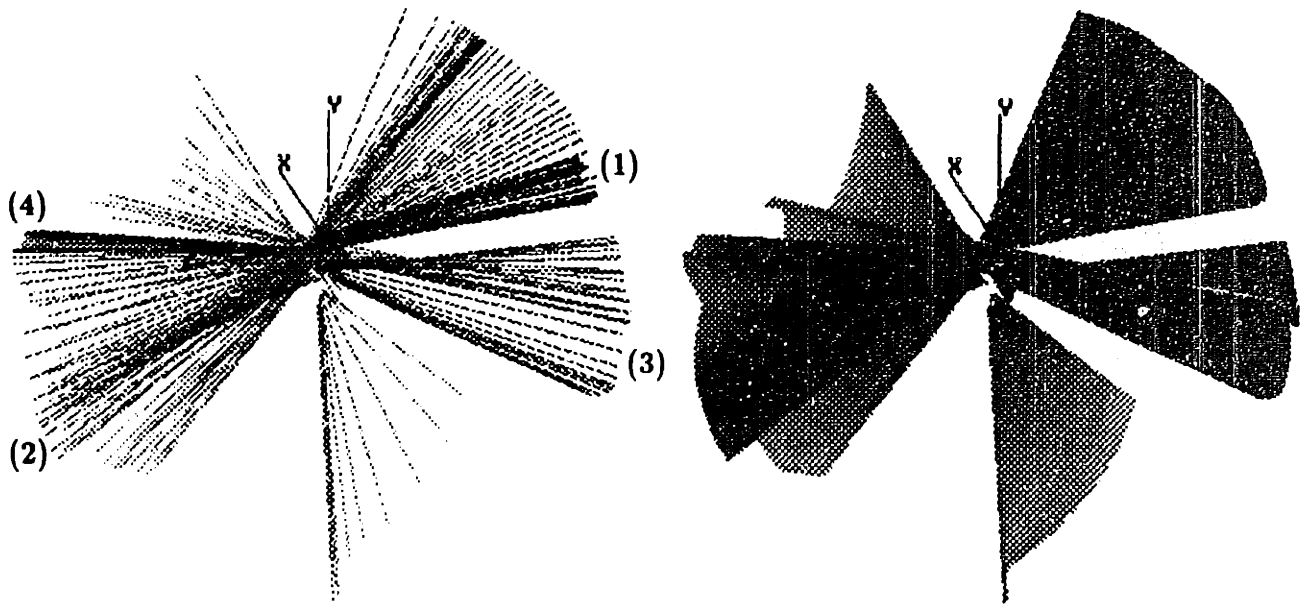

Figure 6.14: Axode for gait, Trial 1 with pin mounting

extension, (2) post-heelstrike flexion, (3) foot flat extension, and (4) toe-off flexion. The initial extension is fairly planar in the beginning, but acquires a significant component of rotation along the positive y-axis just prior to heelstrike (HS). Subsequent to HS, a flexion is observed: the corresponding axode structure is slightly conical, indicating roughly planar motion. The following extension during foot flat (FF) is also slightly non-planar. Prior to toe-off (TO), the observed flexion shows significant three-dimensional motion components; at TO, it becomes planar. Although each of these four structures represents motion which is planar to some degree, each phase of the motion occurs in a different plane. This, taken together with the pre-HS y-rotation, demonstrates that the mechanism for gait is fully three-dimensional, and significantly different from the planar swing mechanism.

Data from Type 2 mounting is shown in Figures 6.15, 6.16, 6.17 (corresponding to gait Trial 4), 6.18, 6.19 and 6.20 (Trial 5); several significant differences from the pin data can be seen.

The extension in FF is absent in the Trial 5 axode (also for other trials not shown); in

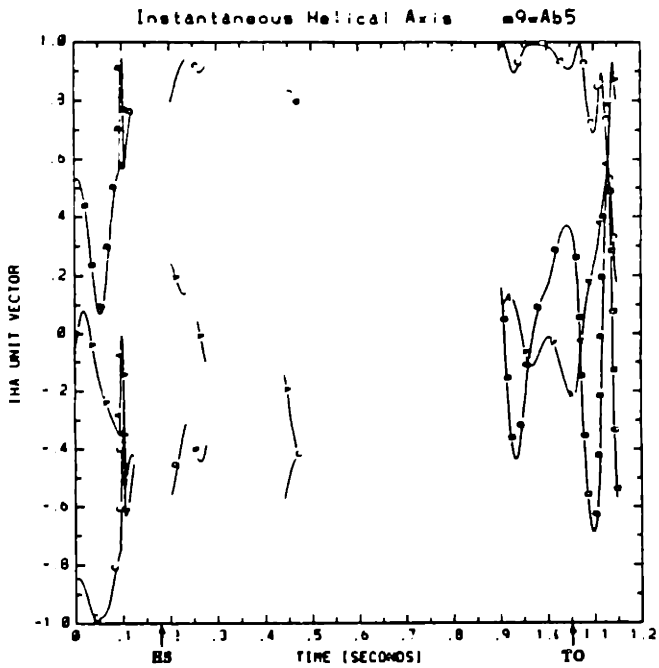

Figure 6.15: IHA direction for gait, Trial 4 with Type 2 mounting

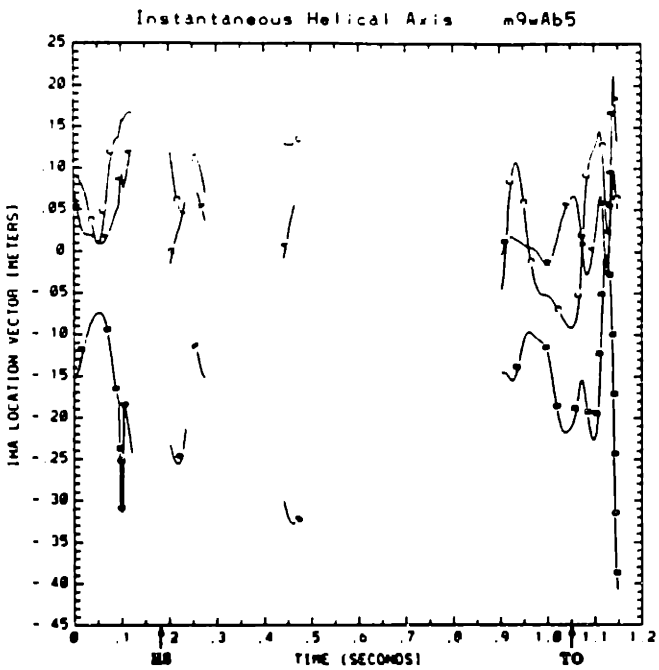

Figure 6.16: IHA location for gait, Trial 4 with Type 2 mounting

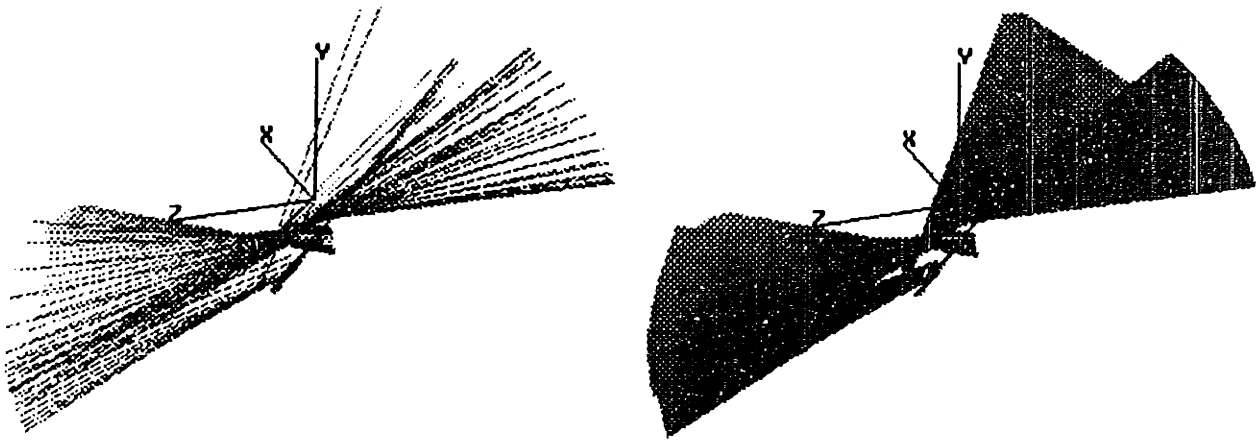

Figure 6.17: Axode for gait, Trial 4 with Type 2 mounting

Trial 4, there is a structure representing a FF extension, but it is almost perpendicular to the corresponding IHA bundle seen in the pin data. Graphs of angular speed versus time (see Figures 6.21 and 6.22 for Trials 4 and 5, respectively) show a peak before TO (at $t \approx 0.5$ s - 0.7 s for Trial 5) in Type 2 data corresponding to a similar peak in the directly measured data (Figure 6.23, $t \approx 0.45$ s - 0.6 s); this peak represents FF extension. However, comparing relative magnitudes of these peaks (with respect to angular speeds at the initial extension and the TO flexion), it is seen that for Type 2 mounting, a lower angular speed is measured during FF extension. Equally important, angular speed cutoff levels (see Section 5.1) are higher for external mounting than for direct mounting, indicating higher error levels in the experiments with skin-mounted arrays. The combination of the lower magnitude of the FF extension angular speed, and the higher error levels, result in the elimination of the corresponding structure in the axode for gait with Type 2 mounting.

A second observation regarding gait measured with Type 2 mounting, is that the axode lies almost entirely in the yz-plane, *i.e.* there is very little rotation in the x-

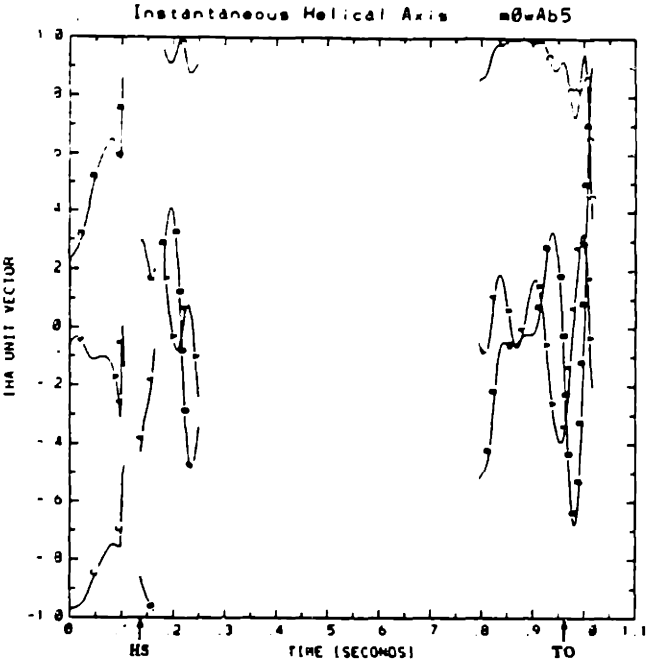

Figure 6.18: IHA direction for gait, Trial 5 with Type 2 mounting

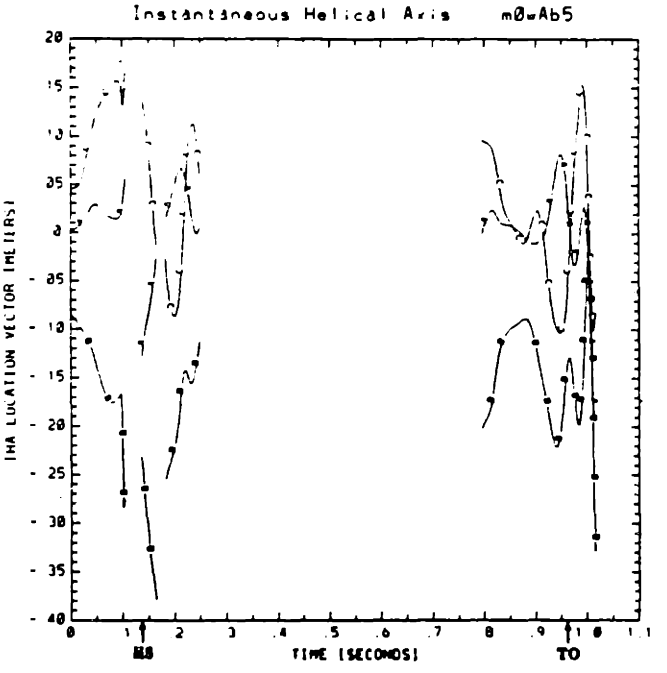

Figure 6.19: IHA location for gait, Trial 5 with Type 2 mounting

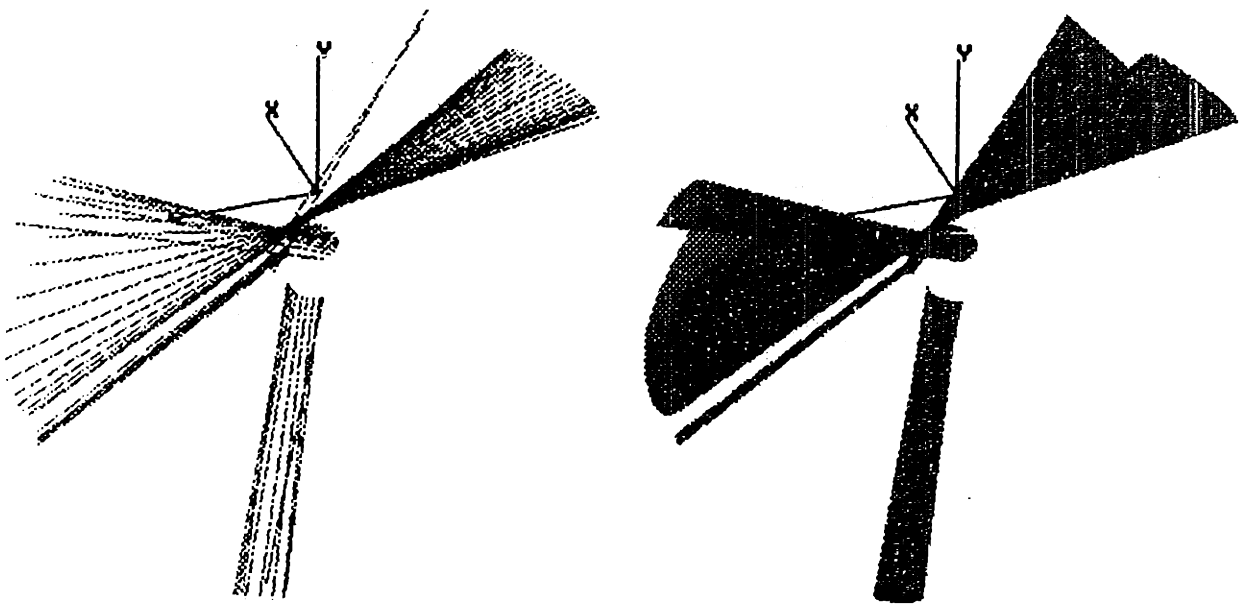

Figure 6.20: Axode for gait, Trial 5 with Type 2 mounting

direction. For the pin data, x-components are seen in the inital extension and the FF extension. It is interesting to note that for Type 2 data, the inital extension in gait has an x-component which is less than the corresponding x-rotation seen in voluntary swing trials, while for pin data the x-component of the initial extension in gait is greater than x-rotation in extension during swing experiments.

Lastly, in several of the trials with Type 2 mounting, a rotation in the negative y-direction is observed immediately following HS, prior to the post-HS flexion (see Fig. 6.18). This structure is not at all present in the pin data. Note that the y-axis, which is approximately parallel to the long axis of the femur, is a likely candidate for an axis of rotation of soft tissue motion. Given the direction of the axode structure together with its timing, it is probable that the observed rotation is artifactual skin motion caused by the impact at HS.

Data from Type 1 mounting does not lend itself easily to analysis. As can be seen in Figures 6.24, 6.25 and 6.26, there are large fluctuations in IHA direction throughout the data set. It is difficult to discern any structures, except for gross motions corresponding

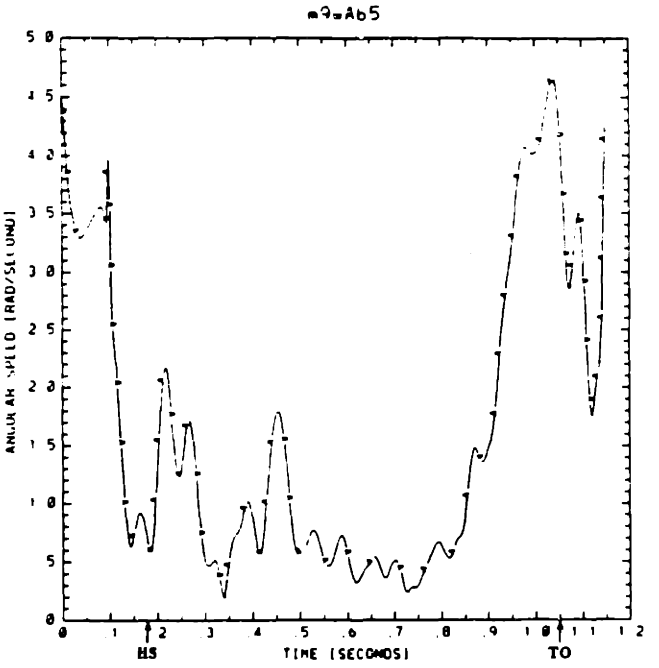

Figure 6.21: Angular speed for gait, Trial 4 with Type 2 mounting

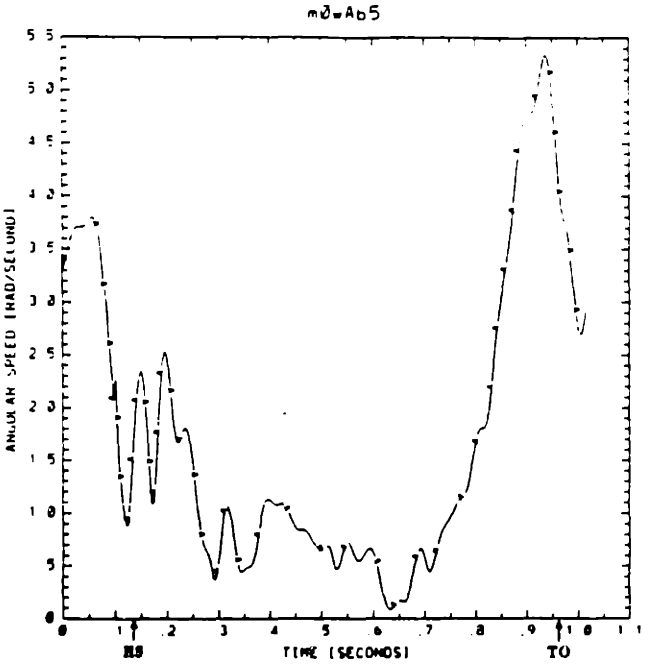

Figure 6.22: Angular speed for gait, Trial 5 with Type 2 mounting

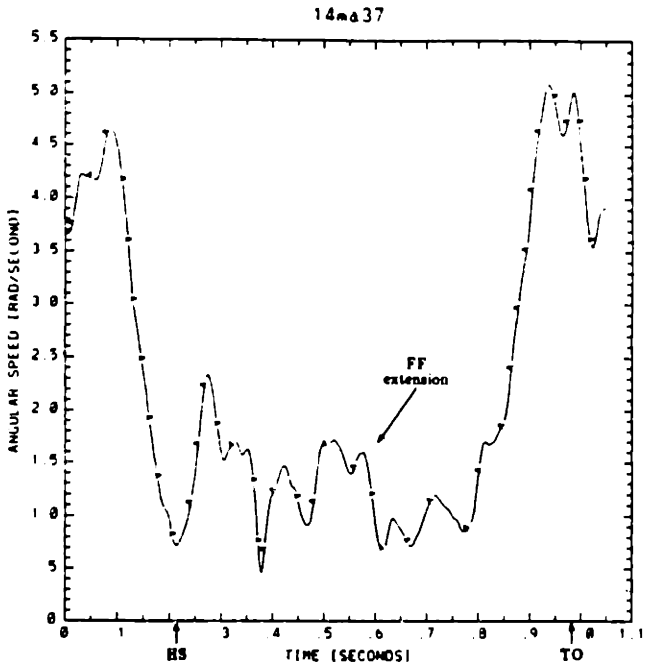

Figure 6.23: Angular speed for gait, pin mounting

to initial extension and TO flexion. The axode suggests fully 3-dimensional motion, but none of the patterns are repeated in other trials. The fluctuations may be due either to array motion with respect to the bone, indicating that Type 1 mounting is sloppy; or measurement errors, such as the reflection problem observed earlier in a swing trial.

Comparing gait axodes for Type 1 and Type 2 mounting with the pin data, several differences are seen. As described previously, measurements using Type 2 mounting do not detect the FF extension. This is partially due to the high error levels, and partially because of the lower angular speed obtained with skin-mounted arrays, which in turn may be an artifact of soft tissue motion. Other discrepancies observed were the magnitudes of the x-component in the initial extension, and the y-rotation immediately after HS present in Type 2 data axodes. Results using Type 1 mounting indicate that this attachment method either increases the probability of severe measurement errors (*e.g.* reflections) or that the mounting method allows for significant array motion with respect to the skeletal segments.

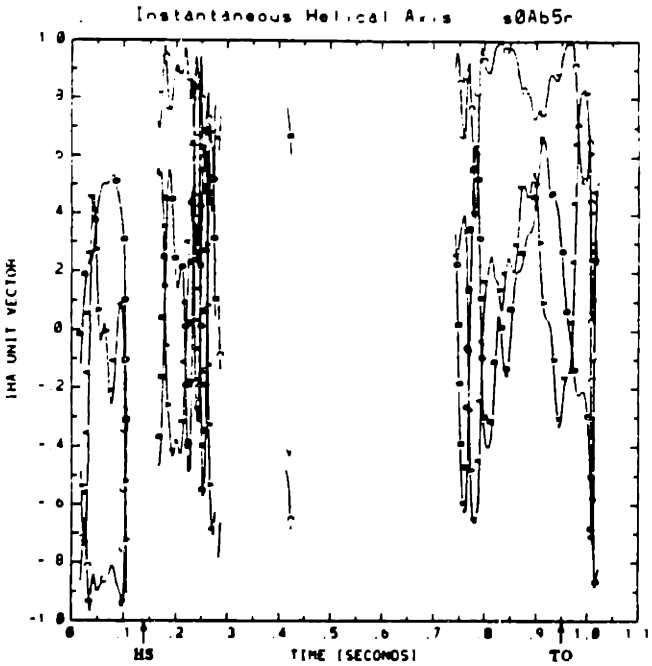

Figure 6.24: IHA direction for gait, Trial 4 with Type 1 mounting

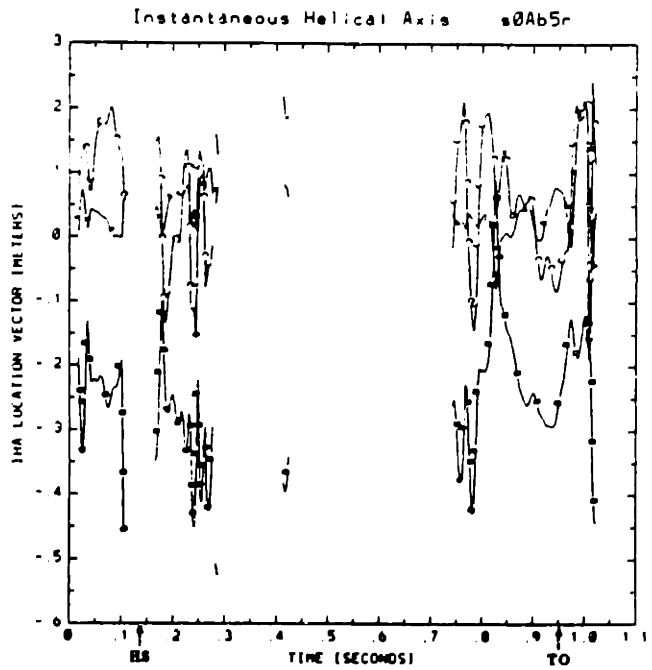

Figure 6.25: IHA location for gait, Trial 4 with Type 1 mounting

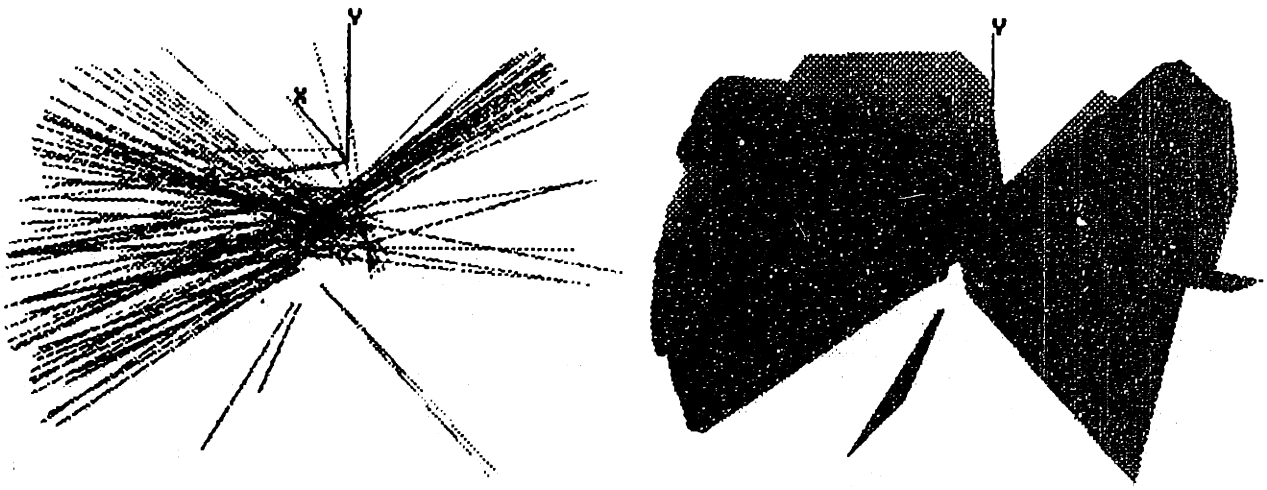

Figure 6.26: Axode for gait, Trial 4 with Type 1 mounting

mounting presented in Section 6.1, an ostensibly small deviation in the 3-D position of an LFD causes a major fluctuation in the calculated IHA.

Despite the sensitivity to noise, it has been shown that axodes can be used to identify the nature of the mechanisms present in various biokinematic experiments, and that one can distinguish between different tasks as well as different mounting methods by comparison of axode shapes.

In conclusion, the results of this research indicate that axodes can be used for analysis and comparison of biokinematic data, but that measurement errors in the presented data are large enough to significantly limit the amount of useful information available in IHA representations.

7.2 Use of Skin-mounted Markers to Measure Skeletal Kinematics

Two different methods for attaching marker arrays on the skin were investigated. Differences between the axode shapes from data measured with externally mounted arrays and from directly measured skeletal motion were observed. Some of these discrepancies could be attributed to motion of the skin-mounted array relative to the underlying skeletal segment.

Type 2 mounting, consisting of molded, plastic forms held in place by vascular stocking, was shown to yield array kinematics only similar in first approximation to the skeletal motion. In swing experiments, skin motion caused cone-like axode structures, indicating deviation from the planar motion seen in the direct measurements. For gait trials, a rotation about the BFCS y-axis was observed immediately after HS. Since the leg would be approximately fully extended at that time, the y-axis is aligned with the long axis of both the femur and tibia. The observed axode structure, then, is consistent with the kinematics that result from torsional motion of muscle mass about the bone.

Externally mounted arrays failed to produce the axode structure corresponding to extension during foot flat. Although the main reason for this is that noise levels in the

data were higher than for the pin experiments, graphs of Ω versus time indicate that with Type 2 mounting, the measured angular speeds of extension were lower than those obtained with directly mounted arrays. This attenuation of array angular speed may be due to soft tissue motion; the effect is to increase errors in Type 2 data to magnitudes above the allowed noise levels.

Type 1 mounting, which used rigid, acrylic frames with elastic straps, produced axodes with very little structure. Large variations in IHA components were observed, especially in gait trials, and axode patterns were not repeatable. The results indicate that this attachment method either allows significant array motion with respect to the skeleton, or that somehow, reflections or other measurement errors are more likely to occur with Type 1 mounting.

7.3 Recommendations

To improve the quality of results, and to increase the usefulness of axode representations, future data must be acquired with higher precision.

One very effective improvement in experimental methodology would be the increase of the number of markers per TRACK array from the current four. Discontinuities were observed in quaternion plots as data from the redundant fourth LED were included or excluded in calculations. Not only does the presence of such discontinuities corrupt velocity estimates, but the relatively large magnitude of the discontinuities indicate that there is significant uncertainty in the least-squares solution of the orientation calculation. More markers per rigid body would increase redundancy, lowering uncertainty. Another testament to the detrimental effect of using few LEDs per array is the fact that estimated error levels for the 1984 study with bone-mounted markers are smaller than the corresponding error estimates for the externally mounted markers. Although the pin data have lower resolution, and were processed using higher cutoff levels for skew ray and inter-LED errors, arrays with 6 LEDs each were used, resulting in error levels superior to those for the 4 LED skin-mounted arrays.

Resolution can be improved by altering experiment geometry. By placing the subject closer to the cameras, a Selspot Unit will correspond to a smaller length in the viewing volume, thus increasing precision of marker position measurements. Also, in the current experimental setup, angular velocity components in the z-direction have higher precision than x- and y-components; however, the subject is oriented so that the flexion-extension axis, about which the highest angular velocities occur, is along the z-axis. This arrangement results in signal-to-noise ratios for x- and y-rotations which are inferior to the signal-to-noise ratio for z-rotations. For improved measurements of the components of angular velocity corresponding to internal/external rotation and adduction/abduction, the TRACK arrays should be placed on the anterior surface of the leg rather than the lateral surface, with the subject facing the cameras.

Reflections were shown to cause potentially large errors. Based on the procedure used in Section 6.1 to identify a probable reflection, the use of cross-correlation calculations between the 3-D trajectories for each LED on an array should be investigated as a possible tool to detect deviations due to reflection of light.

A recent development in opto-electronic technology may significantly improve measurements by virtually eliminating reflection errors. Watsmart (Northern Digital, Waterloo, Ontario, Canada) cameras using linear photo-effect diodes measure (u, v)-coordinates of the location of maximum intensity, rather than the center of intensity. Thus, relections of light from the LEDs will not distort measurements.

Another hardware change which may improve results would be the use of accelerometers to supplement TRACK rigid body data. By providing an additional sensor, which may be integrated to yield velocity information, it is possible that improved derivatives of $\mathbf{x}$ and q result, which in turn would yield more accurate axodes.

Because error levels in the calculated IHA data were substantial, axode shapes were approximate only. Therefore, in this study, axodes were compared qualitatively, by visual inspection. With improved data, quantitative methods of comparing axode shapes would be more appropriate. Ideally, dual curvature and torsion should be calculated, but the

necessary derivative estimates impose unrealistic requirements on precision. However, other quantitative approaches to axode comparison exist. Minimization algorithms may be used to align axodes in a "best-fit"; a measure of closeness of fit would indicate the degree of similarity in shape. Alternatively, one may develop a method of comparison based on cross-correlation techniques.

The use of axodes to compare array attachment methods presumes that for a given subject performing a given task, the mechanism, and thus the axode shape, will be relatively constant. To assess the variations in axode shape due to variations in the mechanism which generates a motion, more experimental data is needed. Repeatability of gait kinematics in consecutive gait cycles can be investigated using the large-volume TRACK system developed by Mansfield [12]. Although evidence in this research suggests that the mechanisms remain fairly constant, this is an area which requires further work.

In conclusion, axodes appear to be a promising method for representing biokinematic data. Although measurement errors in the experiments have limited the amount of useful information in the axodes presented here, significant improvements to the data acquisition system have been made since these experiments were conducted. By additionally implementing some of the above recommendations, better results can be expected in future studies.

Bibliography

[1] Antonsson, E.K. *A Three-Dimensional Kinematic Acquisition and Intersegmental Dynamic Analysis System for Human Motion.* PhD thesis, Massachusetts Institute of Technology, Cambridge, MA, June 1982.

[2] Antonsson, E.K. and Mann, R.W. Automatic 6-d.o.f. kinematic trajectory acquisition and analysis. *J. Dyn. Sys. Meas. and Cont.*, 111:31–39, March 1989. 517.

[3] Dimentberg, F.M. *The Screw Calculus and Its Applications in Mechanics.* Air Force Systems Command, Foreign Technology Division, Wright-Patterson AFB, Dayton, Ohio, 1968. translated from 1965 Russian edition published by Nauka, Moscow.

[4] Dohrmann, C. A dynamic programming approach to smoothing and differentiating data with splines. Master's thesis, The Ohio State University, Columbus, OH, 1986.

[5] Dohrmann, C.R. and Busby, H.R. Algorithms for smoothing noisy data with spline functions and smoothing parameter selection. In *Proceedings of the VIth International Congress on Experimental Mechanics*, June 1988. 419.

[6] Grood, E.S. and Suntay, W.J. A joint coordinate system for the clinical description of three–dimensional motions: Application to the knee. *J. Biomechanical Engineering*, 105:136–144, May 1983. 407.

[7] Hart, R.A., Mote, C.D. and Skinner, H.B. 3-D description of the motion of human knee using the finite helical axis. In *Proc. 35th Annual Meeting*, Las Vegas, Nevada, 1989. Orthopaedic Research Society.

[8] Karlsson, J.O.M. The instantaneous helical axis and its application to motion analysis. Bachelor's Thesis, Massachusetts Institute Technology, Cambridge, Massachusetts, May 1988.

[9] LaFortune, M.A. *The Use of Intra-Cortical Pins to Measure the Motion of the Knee Joint During Walking.* PhD thesis, The Pennsylvania State University, 1984.

[10] Levens, A.S., Inman, V.T. and Blosser, J.A. Transverse rotation of the segments of the lower extremity in locomotion. *J. Bone and Joint Surg.*, 30A(4):859–872, October 1948. 280.

[11] Mansfield, P.K. *TRACK4 User's Manual.* Newman Lab. for Biomech. and Human Rehab., M.I.T., Cambridge, Massachusetts, 1987.

[12] Mansfield, P.K. *A Large Volume Close-range Photogrammetric System.* PhD thesis, Massachusetts Institute of Technology, Cambridge, Massachusetts, May 1990.

[13] Murphy, M.C. *Geometry and the Kinematics of the Normal Human Knee.* PhD thesis, Massachusetts Institute of Technology, Cambridge, Massachusetts, June 1990.

[14] Murphy, M.C. and Mann, R.W. A comparison of smoothing and digital filtering/differention of kinematic data. In *Proc. of the 9th Ann. Conf. of the IEEE Eng. in Med. and Biol. Soc.*, Piscataway, New Jersey, Nov. 1987. vol.12.

[15] Murphy, M.C., Dube, N., Zarins, B., Jasty, M., and Mann, R.W. A comparison of skeletal kinematics measured *in vivo* using different methods for attaching markers: Work in progress. In *Abstracts of the Third Annual East Coast Clinical Gait Laboratory Conference – National Institutes of Health, Bethesda, Maryland*, November 1987. 522.

[16] Murphy, M.C., Karlsson, J.O.M. and Mann, R.W. A comparison of smoothing spline algorithms for obtaining derivatives of noisy kinematic data. In *Abstracts of the 4th Ann. East Coast Clin. Gait Lab. Conf.*, State College, Pennsylvania, 1988. Pennsylvania State University.

[17] Murphy, M.C., Zarins, B., Jasty, M. and Mann, R.W. *In vivo* measurement of the three-dimensional skeletal motion at the normal knee. In R.L. Spilker, editor, *1984 Advances in Bioengineering*, pages 64–65. Amer. Soc. Mech. Eng., 1984. 378.

[18] Rowell, D. and Mann, R.W. Human movement analysis. *SOMA*, 3(2), Spring 1990.

[19] Schut, G.H. On exact linear equations for the computation of the rotational elements of absolute orientation. *Photogrammetria*, 17(1):34–37, 1960/61. 527.

[20] Shiavi, R.S., Limbird, T., Frazer, M., Stivers, K., Strauss, A. and Abramovitz, J. Helical motion analysis of the knee – II. kinematics of uninjured and injured knees during walking and pivoting. *J. Biomechanics*, 20(7):653–665, 1987. 320.